Ⓔ

DYNAMICAL AND PHYSICAL PROPERTIES OF A POST–CORONAL MASS EJECTION CURRENT SHEET

YUAN-KUEN KO,[1] JOHN C. RAYMOND,[1] JUN LIN,[1] GARETH LAWRENCE,[2] JING LI,[3] AND ANDRZEJ FLUDRA[4]

ABSTRACT

In the eruptive process of the Kopp-Pneuman type, the closed magnetic field is stretched by the eruption so much that it is usually believed to be " open " to infinity. Formation of the current sheet in such a configuration makes it possible for the energy in the coronal magnetic field to quickly convert into thermal and kinetic energies and cause significant observational consequences, such as growing postflare/CME loop system in the corona, separating bright flare ribbons in the chromosphere, and fast ejections of the plasma and the magnetic flux. An eruption on 2002 January 8 provides us a good opportunity to look into these observational signatures of and place constraints on the theories of eruptions. The event started with the expansion of a magnetic arcade over an active region, developed into a coronal mass ejection (CME), and left some thin streamer-like structures with successively growing loop systems beneath them. The plasma outflow and the highly ionized states of the plasma inside these streamer-like structures, as well as the growing loops beneath them, lead us to conclude that these structures are associated with a magnetic reconnection site, namely, the current sheet, of this eruptive process. We combine the data from the Ultraviolet Coronagraph Spectrometer, Large Angle and Spectrometric Coronagraph Experiment, EUV Imaging Telescope, and Coronal Diagnostic Spectrometer on board the *Solar and Heliospheric Observatory*, as well as from the Mauna Loa Solar Observatory Mark IV K-coronameter, to investigate the morphological and dynamical properties of this event, as well as the physical properties of the current sheet. The velocity and acceleration of the CME reached up to 1800 km s^{-1} and 1 km s^{-2}, respectively. The acceleration is found to occur mainly at the lower corona ($<2.76\ R_{\odot}$). The post-CME loop systems showed behaviors of both postflare loops (upward motion with decreasing speed) and soft X-ray giant arches (upward motion with constant speed, or acceleration) according to the definition of Švestka. In the current sheet, the presence of highly ionized ions, such as Fe^{+17} and Ca^{+13}, suggests temperature as high as $(3–4) \times 10^6$ K, and the plasma outflows have speeds ranging from 300 to 650 km s^{-1}. Absolute elemental abundances in the current sheet show a strong first ionization potential effect and have values similar to those found in the active region streamers. The magnetic field strength in the vicinity of the current sheet is found to be of the order of 1 G.

Subject headings: Sun: corona — Sun: coronal mass ejections (CMEs)

On-line material: color figures

1. INTRODUCTION

Coronal mass ejections (CMEs) are powerful, transient expulsions of coronal material into interplanetary space. Since the launch of the *Solar and Heliospheric Observatory* (*SOHO*), a large number of CMEs have been observed, from their initiation at the solar surface to the propagation through the corona into interplanetary space. Because of their intimate association with the solar cycle and their potentially strong effect on the space environment at the Earth, CME study has been a very vigorous field in both observational and theoretical research.

There are in general two types of origin for CMEs. One is the filament or prominence eruption from quiet-Sun regions that usually contains cool chromospheric material and exhibits complex twisting structure. The other is a more powerful eruption from active regions often associated with

flares, solar energetic particles, and radio bursts. Filaments sometimes also constitute part of the CME from active regions. There have been many multiwavelength studies of individual CME events and statistical studies of the CME properties (e.g., Howard et al. 1985; Hundhausen, Burkepile, & St. Cyr 1994; Goldstein, Newgebauer, & Clay 1998; Innes et al. 1999; St. Cyr et al. 1999, 2000; Ciaravella et al. 2000; Akmal et al. 2001; Gopalswamy et al. 2001). Many efforts have been made to model CME eruption processes in an attempt to understand their initiation, explain the observed structure and dynamical properties, and model their propagation in the heliosphere (e.g., Mikić & Linker 1994; Chen 1996; Antiochos, DeVore, & Klimchuk 1999; Amari et al. 2000; Lin & Forbes 2000; Low 2001; Riley et al. 2002; Manchester et al. 2003; for reviews, see, e.g., Wu, Andrews, & Plunkett 2001).

The generally accepted explanation for the energy source of eruptive phenomena in the solar atmosphere, such as solar flares, eruptive prominences, and CMEs, is the energy stored in the coronal magnetic field prior to the eruption. These eruptive phenomena commonly involve fast mass ejections and intense heating, which imply rapid dissipation of the magnetic energy. In the coronal environment, the electrical conductivity of the plasma and the length scale of the magnetic field are fairly large, so rapid dissipation of the magnetic field is almost impossible (e.g., Priest 1982; Priest

[1] Harvard-Smithsonian Center for Astrophysics, 60 Garden Street, Cambridge, MA 02138.

[2] Center for Solar Physics and Space Weather, Catholic University of America, Washington, DC 20064.

[3] Institute for Astronomy, University of Hawaii, 2680 Woodlawn Drive, Honolulu, HI 96822.

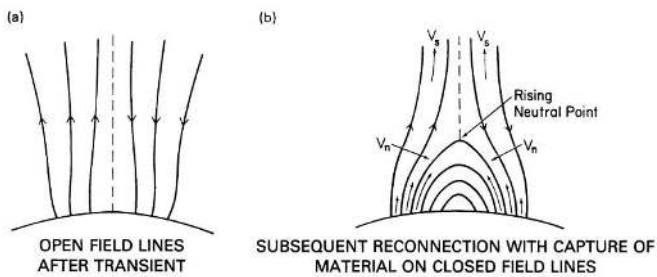[4] Rutherford Appleton Laboratory, Chilton, Didcot, Oxfordshire 0X11 0QX, UK.

Fig. 1.—Postflare/CME loop model by Kopp & Pneuman (1976). (*a*) The magnetic field is pushed open by an eruption, and a current sheet separates two antiparallel magnetic field lines. (*b*) The opened configuration relaxes into a closed, nearly potential field via the magnetic reconnection in the current sheet. This process produces two bright and separating flare ribbons on the solar disk and a continually growing flare loop system in the corona (reproduction of Fig. 1 of Kopp & Pneuman 1976).

& Forbes 2000) unless the magnetic configuration includes some neutral regions, such as neutral point, null point, current sheet, or quasi-separatrix layers (e.g., Démoulin et al. 1996; Priest & Forbes 2000), in which the fast magnetic reconnection can occur easily.

Kopp & Pneuman (1976) proposed a scenario for two-ribbon flares (Fig. 1; the idea was raised by Carmichael 1964 for the first time.) In this model, energy is stored in a force-free magnetic arcade or flux rope prior to the eruption. Eventually, the field erupts to form a fully open magnetic configuration including a neutral current sheet that separates two antiparallel magnetic field lines (Fig. 1*a*). Finally, the open configuration relaxes into a closed, nearly potential field via magnetic reconnection in the current sheet, and the magnetic energy is converted into kinetic and thermal energies (Fig. 1*b*). The observational consequences of this process are two bright and separating flare ribbons on the solar disk and a continually growing flare loop system in the corona. The motions of the flare ribbons and loops are not due to mass motions of the plasma but to the upward propagation of the energy source onto new magnetic field lines at higher altitude (Schmieder et al. 1987). According to Figure 1, the upward propagation of the energy source implies continuous erosion of the current sheet due to reconnection. As pointed out by Forbes (2000), images obtained from *Yohkoh* Soft X-ray Telescope (SXT) provide many pieces of evidence that suggest magnetic reconnection in the corona during an eruption. These include a hard X-ray source located above the soft X-ray loops (Sakao et al. 1992; Masuda et al. 1994; Bentley et al. 1994), cusp structure suggesting either an X-type or a Y-type reconnection site (Acton et al. 1992; Tsuneta 1993; Doschek, Strong, & Tusneta 1995), bright features at the top of the soft X-ray loops (Tsuneta et al. 1992; McTiernan et al. 1993), and high-temperature plasma along the field lines mapping to the tip of the cusp (Tsuneta 1996). Recently, Yokoyama et al. (2001) reported the observation of plasma inflow merging to a local area above the cusp structure.

Observations show that bright ribbons and loops can last for more than 10 hr (e.g., Švestka 1976). Ribbons and loops appear to move through the chromosphere and the corona, and the outermost edges of the hot loops map to the outer edge of the flare ribbons (Schmieder et al. 1996; Antiochos et al. 2000), while the cool Hα loops map to the inner edge of the ribbons (Rust & Bar 1973). According to the models, the hot loops are the newly reconnected closed loops, which

are heated by shocks due to reconnection (Forbes, Malherbe, & Priest 1989). The cool loops, which lie inside the hot loops, are formed from the hot loops by radiative cooling (Švestka et al. 1987; Forbes & Acton 1996). Observations supporting this scenario include rising X-ray loops (e.g., Švestka 1996), cool loops lying inside the hot loops (e.g., McCabe 1973; Švestka et al. 1987; Schmieder et al. 1996), and Dopper shift measurements (Schmieder et al. 1987) providing evidence of chromospheric evaporation. The density of the postflare loops was found to be a few times 10^{10} cm^{-3} in the X-ray/EUV loops (e.g., Withbroe 1978) and as high as 10^{12} cm^{-3} in the Hα loops (e.g., Heinzel & Karlický 1987). Both are much denser than what is found above nontransient solar structure, which is generally below 10^9 cm^{-3} just above the solar surface (e.g., Guhathakurta & Fisher 1995; Parenti et al. 2000).

Recent research indicates that the closed magnetic field does not necessarily become fully open as the Kopp-Pneuman–type eruption occurs. Instead, the magnetic structure is highly stretched by the eruption, and a current sheet forms (see Fig. 2). Both numerical simulations and analytical studies show that when the footpoints of a closed magnetic structure are sheared (Mikić & Linker 1994), or the whole structure is stretched outward by the catastrophic loss of equilibrium in a magnetic flux rope (Forbes & Isenberg 1991; Isenberg, Forbes, & Démoulin 1993; Forbes & Priest 1995), a current sheet develops in the stretched configuration. With dissipation in the current sheet, the stretched magnetic field lines start to reconnect, producing new closed field lines below the current sheet, so the preexisting closed magnetic field never becomes fully open. There are several ways to trigger dissipation in the current sheet. The current sheet is subject to the tearing mode instability, and magnetic reconnection occurs as soon as the length of the current sheet becomes longer than $\sim 2\pi$ times its width (Furth, Killen, & Rosenbluth 1963). Alternatively, as the current sheet builds up, its current density may exceed the threshold of a micro-instability, which creates anomalous resistivity (Galeev & Zelenyi 1975; Heyvaerts & Priest 1976) and triggers rapid reconnection. The scenario sketched by Figure 2 suggests that the role played by reconnection in an eruptive process is twofold. First, reconnection breaks the magnetic field lines that pass over the flux rope and are anchored in the boundary surface at both ends. These field lines produce strong magnetic tension force in a stretched configuration that would otherwise prevent the flux rope from escaping to form a CME. Second, reconnection dumps large amounts of energy in the lower atmosphere of the Sun, creating intense heating, which accounts for the traditional flare ribbons and loops. Figure 2 incorporates the flare models summarized by Forbes & Acton (1996) and the CME model of Lin & Forbes (2000, hereafter LF00). It clearly illustrates the relationship among solar flare, eruptive prominence, and CME and suggests that *these three eruptive phenomena are actually different manifestations of a single physical process that involves a disruption of the coronal magnetic field.*

One of the most significant predictions of the LF00 model is that a current sheet develops following the onset of the eruption. Because the timescale of reconnection is long compared with the timescale of the onset stage (Alfvén timescale), dissipation of the current sheet by reconnection is slow, so the current sheet is able to become fairly long. The evolution of the current sheet is significantly constrained by the local Alfvén speed. In an isothermal corona, the local
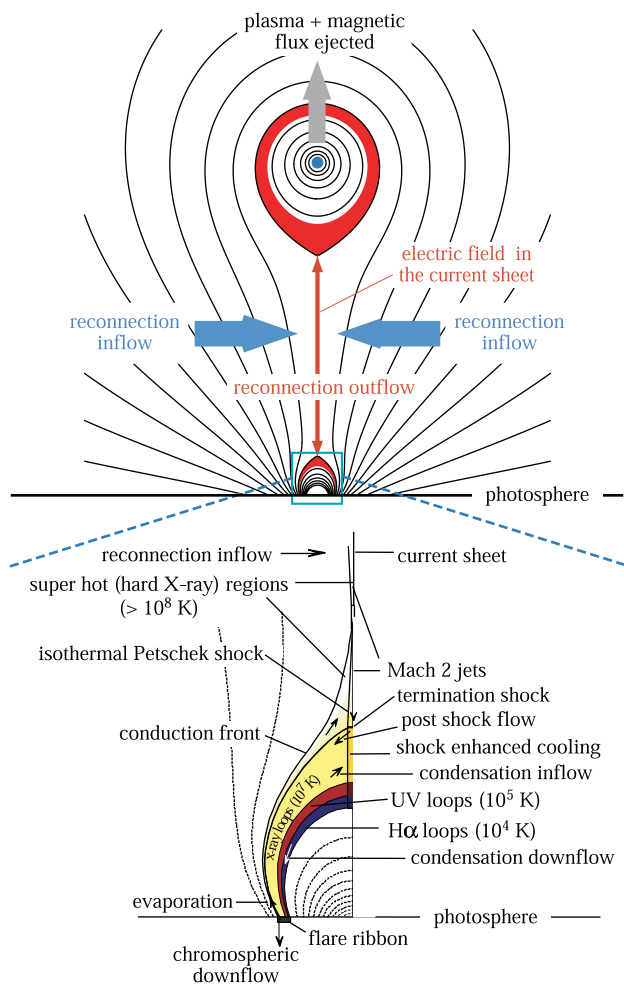
Fig. 2.—*Upper part:* Sketch of the flux rope/CME model of Lin & Forbes (2000) showing the eruption of the flux rope, the current sheet formed behind it, and the postflare/CME loops below, as well as the inflows and outflows associated with the reconnection. *Lower part:* Enlarged view of the postflare/CME loops (adopted from Forbes & Acton 1996). The upper tip of the cusp rises as reconnection happens continuously.

Alfvén speed increases with height at large altitudes, so the current sheet is quickly eroded by reconnection, and its length consequently shrinks several hours after the onset (LF00; Forbes & Lin 2000). In a more realistic corona, on the other hand, the local Alfvén speed decreases with height at large altitudes; erosion of the current sheet is thus not very fast, and the current sheet may remain a long time (Lin 2002, hereafter Lin02). The model predicts that the magnetic energy around the current sheet is converted into kinetic and thermal energy of the plasma during the reconnection process. The plasma then flows along the current sheet both upward and downward at approximately the Alfvén speed and is heated to high temperature inside the current sheet (compared to the ambient corona). The model also predicts certain dynamical properties of the CME and the current sheet that we will discuss in detail in a later section.

There is, however, little direct observational evidence that can confirm the occurrence of the current sheet. The high electrical conductivity and nearly force free environment confine the current sheet to a very local region in the direction perpendicular to its vertical extent (refer to Fig. 2). Therefore, its thickness is so small that we usually treat the current sheet as an infinitely thin layer. In addition, the low plasma density in the corona implies that the plasma inside the current sheet should be tenuous. Therefore, it is difficult to observe the current sheet in an eruptive process because both its size and emission are easily dominated by other large-scale and bright structures nearby. Ciaravella et al. (2002) analyzed the spectral data obtained from the Ultraviolet Coronagraph Spectrometer (UVCS; Kohl et al. 1995) on *SOHO* after an eruption on 1998 March 23. After the bulk CME material left the inner corona, a bright postflare/CME arcade was seen by the EUV Imaging Telescope (EIT) and *Yohkoh*/SXT. UVCS detected a very narrow and hot feature that was most prominent in the [Fe xviii] emission in the space between the arcade and the CME core. The appearance of the [Fe xviii] emission means a temperature as high as 6×10^6 K in that area (Ciaravella et al. 2002). Their result is quite consistent with the theoretical expectations of the current sheet in the flux rope model sketched in Figure 2. Webb et al. (2003) analyzed 26 " candidate disconnection events " (CDEs) associated with CMEs observed by the *Solar Maximum Mission* (*SMM*). These CDEs were followed by raylike structures that appeared a few hours after the CDE and sometimes were found to connect to newly formed streamers close to the limb. They regard this kind of raylike structures as evidence of the current sheet developed following a CME (cf. Fig. 2).

A recent eruption provides us with a unique opportunity for scrutinizing the current sheet as well as the global morphological features of the eruption. This eruption occurred at the east limb of the Sun on 2002 January 8. The CME left behind some long and thin streamer-like structures with continuous outflows as seen in white light. Lower in the corona, UV/EUV observations showed formation of the post-CME loops, and an electron temperature of $(3–4) \times 10^6$ K was found at 1.53 $R_\odot$. Temperatures this high at this height are not commonly seen in the quiescent corona, even above most active regions (Ciaravella et al. 2002). We believe that these streamer-like structures consist of a current sheet in which the magnetic reconnection occurs. The observed high temperature results from the heating in the magnetic reconnection processes that also produce continuous outflows along the current sheet and the formation of the post-CME loops beneath it. In many respects, this eruption is like many observed previously, but the location of the source region (AR 9782/9785; see the next section) and the orientation of the disrupted magnetic configuration lead to a current sheet just along the line of sight (i.e., edge-on), as illustrated in Figure 2. This makes it possible for us to analyze the plasma properties and investigate the evolution of the current sheet, as well as the post-CME loops below it. In the next section, we describe this event as observed in white light and UV/EUV and find many aspects consistent with the predictions of the models described in this section. In § 3, we analyze the dynamical and physical properties of this current sheet and interpret the data based on the work by LF00 and Lin02. Finally, we summarize our analysis in § 4.

2. THE OBSERVATIONS

We suggested in the previous section that solar flares, eruptive prominences, and CMEs are different manifestations of

a single physical process that involves a disruption of the coronal magnetic field followed by magnetic reconnection. In this section, we describe a CME followed by the formation of the post-CME loops and the current sheet that provides good illustration of this idea. This event was observed by the Large Angle and Spectrometric Coronagraph Experiment (LASCO; Brueckner et al. 1995), EIT (Delaboudinière et al. 1995), UVCS, and Coronal Diagnostic Spectrometer (CDS; Harrison et al. 1995) on board *SOHO* as part of *SOHO* Joint Observing Program 151, as well as by the Mauna Loa Solar Observatory (MLSO) Mark IV K-coronameter (MK4). Because of the dynamical nature of all eruptions, it may be helpful to refer to the movies[5] of this event recorded by *SOHO*/LASCO and *SOHO*/EIT.

2.1. *The Coronal Mass Ejection and the Current Sheet*

On 2002 January 8, a major eruption occurred at the east limb of the Sun. The corresponding source active region (see § 2.4) was located just behind the limb. Therefore, it is unclear whether a filament preexisted in the relevant magnetic configuration and erupted or whether this eruption started with a flare. The movie obtained by EIT 195 Å shows movement/expansion of the coronal loops that took place for a few hours before the eruption was clearly seen at 17:36 UT. In the image one frame before (17:24 UT), there is some clearer signature of the expansion of the magnetic arcade. Figure 3 shows the CME on the composite image of EIT 195 Å running difference at 18:24 UT and LASCO C2 at 18:30 UT. The overall coronal disruption due to the CME eventually spanned 180° between the two poles by 18:54 UT. Figure 4 is the height-time plot of the leading edge of the CME. The leading edge of the CME first appeared in the LASCO C2 field of view (FOV) at 2.76 $R_\odot$,

---

[5] Available at http://lasco-www.nrl.navy.mil/daily_mpg.
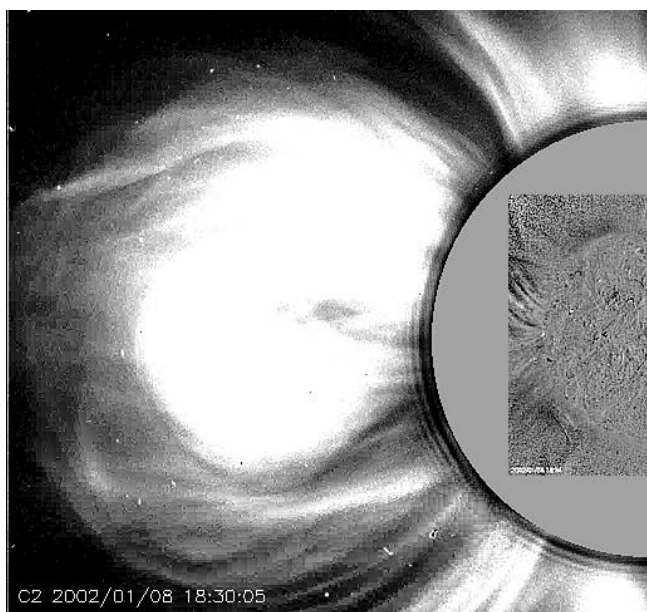

Fig. 3.—Composite image from EIT 195 Å running difference at 18:24 UT, and LASCO C2 at 18:30 UT, showing the 2002 January 8 CME eruption. The nonradial expansion of the field lines in this CME extended from the solar surface well into the outer corona. [*See the electronic edition of the Journal for a color version of this figure.*]
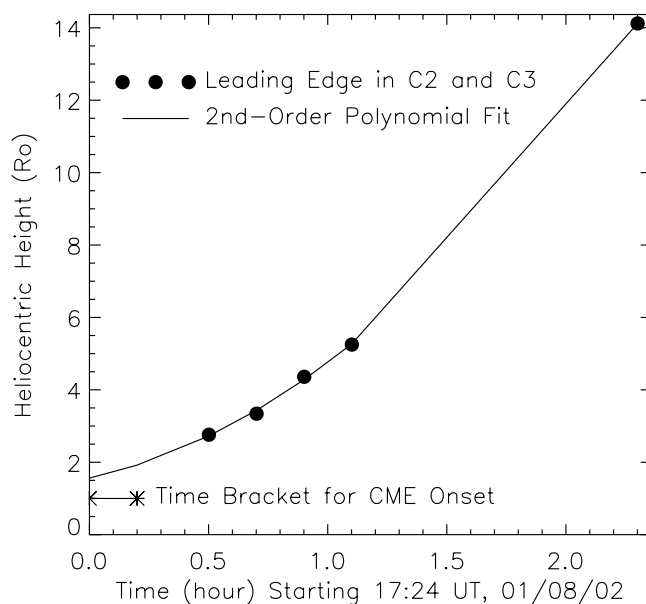

Fig. 4.—Height-time plot (*filled circles*) of the leading edge of the CME measured in LASCO C2 and C3 with the fitting curve of a second-order polynomial (*solid line*). A constant acceleration of 0.19 km s^{-2} provides a good fit to the data. Also plotted is the time frame that brackets the CME onset time, indicating a larger acceleration of $\sim$1 km s^{-2} in the lower corona below 2.76 $R_\odot$.

17:54 UT. It then subsequently traveled to 3.34 $R_\odot$ at 18:06 UT, 5.25 $R_\odot$ at 18:30 UT, and 14.12 $R_\odot$ (in C3) at 19:42 UT. These data points fit well to a curve that corresponds to a constant acceleration rate of about 0.19 km s^{-2}. Furthermore, from this curve, we can evaluate the tangents at points and infer speeds of, for example, around 700 km s^{-1} at 3 $R_\odot$ to over 1800 km s^{-1} by 14 $R_\odot$. This is a fast CME by comparison with the overall CME population (St. Cyr et al. 2000).

We note that with this constant acceleration rate, the time when the CME started would be much earlier than as observed in EIT. Therefore, there must be a different acceleration rate beneath the C2 occulting disk. Also plotted on Figure 4 are two points bracketing the time frame when this CME probably started (between 17:24 and 17:36 UT of EIT images). Taking 17:30 UT as the CME initiation time, we obtain an average acceleration of about 1 km s^{-2} between 1 and 2.76 $R_\odot$. This implies that the CME underwent a much larger acceleration in the lower corona than that seen in LASCO C2. Previous studies found low-coronal accelerations of as much as 2–7 km s^{-2} (e.g., Zhang et al. 2001; Alexander, Metcalf, & Nitta 2002). Using low-corona data of MLSO MK3 and MK4, along with the *SMM* and LASCO data to the outer corona, Burkepile et al. (2002) found that the largest CME acceleration occurs in the low corona (<2.9 $R_\odot$).

After the front of this fast CME had passed, thin threads of streamer formed behind it at a position angle (P.A.) of $\sim$101°, as indicated by the arrow in the upper left panel of Figure 5. Blobs of material can be seen flowing along the streamer continuously as it gradually moved northward (Figs. 5, 6, and 7). We interpret this thin streamer as the current sheet left behind the CME. The blobs are the plasma outflow that is produced by magnetic reconnection in the current sheet (see § 1). They result from the magnetic
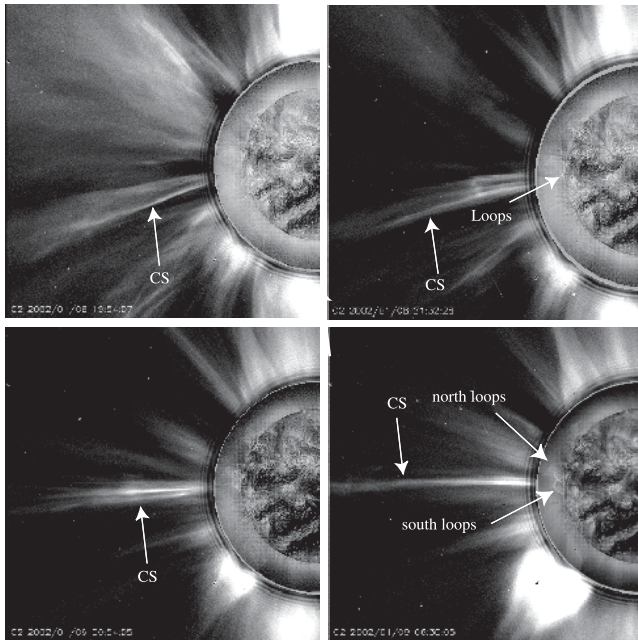
FIG. 5.—EIT and LASCO C2 composite images showing the evolution of the current sheet feature and the post-CME loops. *Upper left:* EIT 195 Å at 19:48 UT, C2 at 19:54 UT, January 8. The arrow points to the current sheet feature (CS) at its early appearance. *Upper right:* EIT 195 Å at 21:17 UT, C2 at 21:32 UT, January 8. The arrows point to the first appearance of the post-CME loops in the EIT image and the current sheet feature. *Lower left:* EIT 195 Å at 00:48 UT, C2 at 00:54 UT, January 9. *Lower right:* EIT 195 Å at 06:24 UT, C2 at 06:30 UT, January 9. The arrows point to the north and south post-CME loop systems. Note that the EIT image is not to scale with C2 in order to show the feature near the limb more clearly (see also Fig. 9 for enlarged EIT images). [*See the electronic edition of the Journal for a color version of this figure.*]
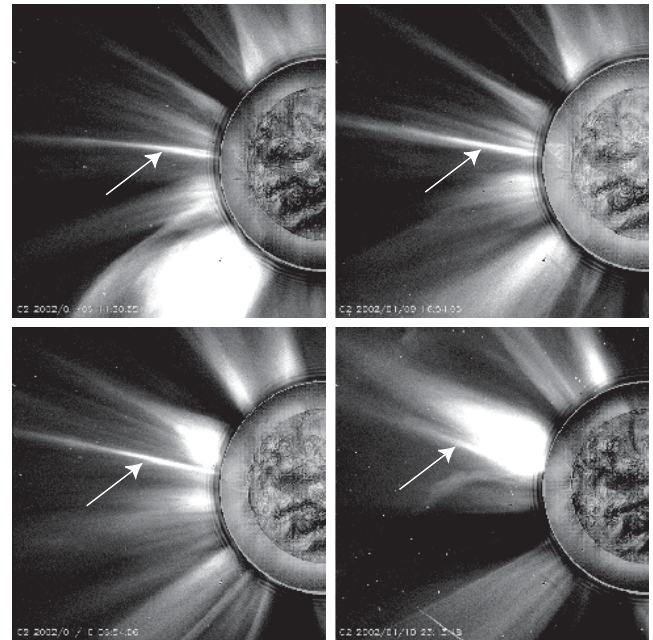

FIG. 6.—EIT and LASCO C2 composite images showing the evolution of the current sheet feature (indicated by the arrow) and the post-CME loops. *Upper left:* EIT 195 Å 11:24 UT, LASCO C2 at 11:30 UT, January 9. *Upper right:* EIT 195 Å at 16:48 UT, C2 at 16:54 UT, January 9. *Lower left:* EIT 195 Å at 06:48 UT, C2 at 06:54 UT, January 10. *Lower right:* EIT 195 Å at 23:18 UT, C2 at 23:13 UT, January 10. Note that the EIT image is not to scale with C2 in order to show the feature near the limb more clearly (see also Fig. 9 for enlarged EIT images). [*See the electronic edition of the Journal for a color version of this figure.*]

reconnection in the nonuniform plasma and the magnetic field.

Several other CMEs occurred after this January 8 CME event. Particularly, a CME from the east limb at 12:06 UT of January 10 seems to push this current sheet farther northward. In addition, a bright streamer started to appear at the northeast limb on January 10 and overlapped with this current sheet feature on the plane of the sky (see Fig. 6, *lower panels*). However, as we examine the C2 running difference images, we find that this current sheet feature preserved its general morphology despite this January 10 CME, and it appeared to be a separate feature, distinct from the bright streamer to its north (Fig. 8).

2.2. *Post-CME Loops*

The post-CME loops started to appear in EIT at around P.A. $\sim 90°$ at 21:17 UT, January 8, as indicated by the arrow in the top left panel of Figure 9. After that, a series of loops appeared at the limb and successively appeared at higher altitude (see Fig. 9). They gradually faded on January 10. This indicates continuous reconnection along the current sheet as described in § 1 to power the flare loops. These loops appear to be in two groups as can be seen from Figure 9 (e.g., indicated by the two arrows in the middle left and bottom left panels). Figure 10 shows the MLSO MK4 white-light image on 17:52 UT of January 9 (*left panel*) and a composite image of EIT (at 17:36 UT), MK4 (at 17:52 UT), and LASCO C2 (at 17:54 UT) (*right panel*). It is

obvious that the thin streamer of interest (i.e., the current sheet feature at P.A. $\sim 83°$) seen in C2 is associated with the southern part of the loop system. We note that the appearance of the two loop systems in the MK4 image (see the inset in the left panel of Fig. 10) is similar to the giant X-ray loops/cusp formed after a flare/CME (e.g., Tsuneta 1996), and the thin feature above the southern loop resembles and is along the same direction as the streamer/current sheet feature seen in LASCO C2. Since the density inside the cusp is expected to be higher than that in the ambient corona (see § 1), the "loop" seen in the MK4 image may actually be the white-light counterpart of the X-ray loops/cusp. However, it is not easy to definitely associate the north loop system seen in MK4 and EIT with structures seen in C2, although it is possible that it is associated with the two thin "spikelike" streamers just north of the long current sheet of interest. This "fan" of spikes seen in C2 (cf. also Figs. 5 and 6) seems to be analogous to the "fan of spikelike rays" seen above the flare loops by *Yohkoh* SXT (McKenzie & Hudson 1999). The latter was found to have a one-to-one association with the X-ray loops in the flare arcade and was interpreted as the current sheet, consistent with the standard reconnection picture.

Figure 11 plots the height versus time of the outer edge of the two post-CME loop systems measured from the EIT images. The measurements end when the top of the loops is out of the EIT FOV (in the case of the north loops) or the loops are too faint to be visible (in the case of the south loops). These loop systems seem to show behaviors of both the postflare loops (the south loops, upward motion with decreasing speed) and the soft X-ray giant arches (the north
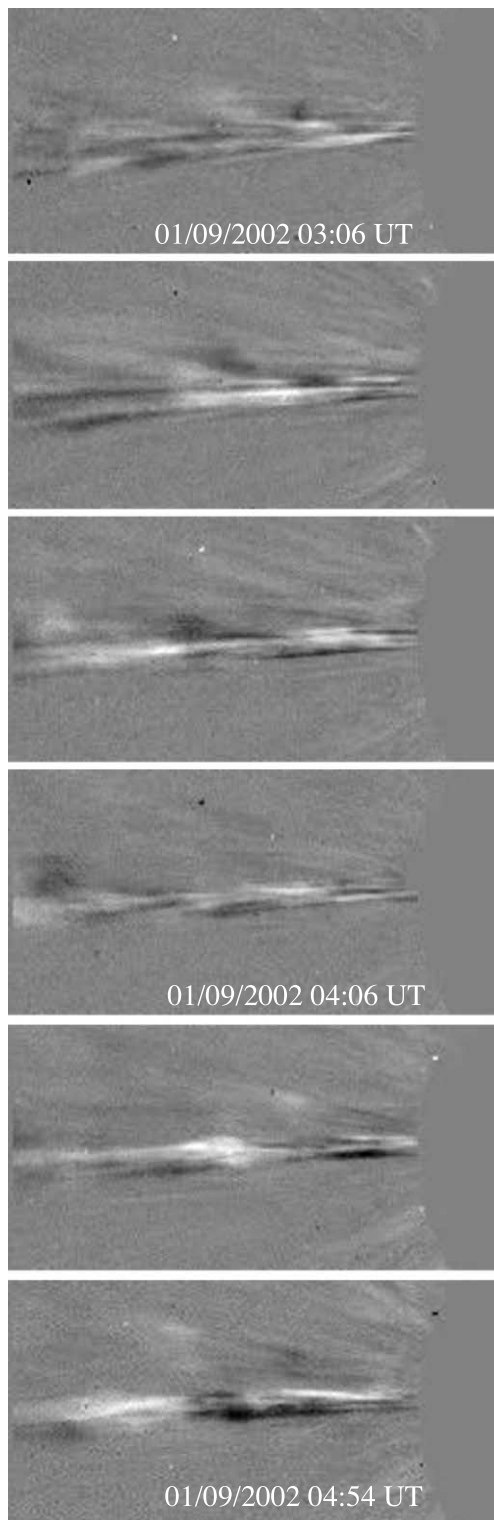
FIG. 7.—Six consecutive LASCO C2 running difference images from 03:06 UT to 04:54 UT of January 9 showing continuously appearing blobs flowing along the current sheet feature at P.A. ∼ 89°.

FIG. 8.—LASCO C2 running difference images showing the current sheet feature at P.A. ∼ 78°. *Left:* at 16:54 UT, January 10; *middle:* at 23:13 UT, January 10; *right:* at 02:30 UT, January 11. The current sheet persisted even after a CME eruption at 12:06 UT, January 10, although it was pushed a bit to the north. It gradually dissipated on January 11.

(less than 5% when ±1 day to the limb as in this case) compared with the growth of the rising loops. The MK4 images may be used to roughly estimate the height of the "loops." We find that at 17:52 UT of January 9, the north loop (see Fig. 10) is at ∼1.7 $R_\odot$ and the south loop is at ∼1.4 $R_\odot$. Note that if the white-light loops indeed correspond to the X-ray

FIG. 9.—EIT 195 Å images showing a more detailed view of the evolution of the post-CME loops. These loops first appeared in the EIT image at 21:17 UT, January 8 (indicated by the arrow in the top left panel), and seem to be in two groups (indicated by the arrows in the middle left and bottom left panels). The subsequent appearance of loops toward higher height implies continuous magnetic reconnection.

loops, upward motion with constant speed, or acceleration) as defined by Švestka (1996). The former group of loops approached the height of 0.3 $R_\odot$ above the solar limb over a period of 40 hr, and the latter group of loops rose above 0.4 $R_\odot$ above the limb over a period of ∼20 hr and appeared to continue growing. Note that the projection effect is small

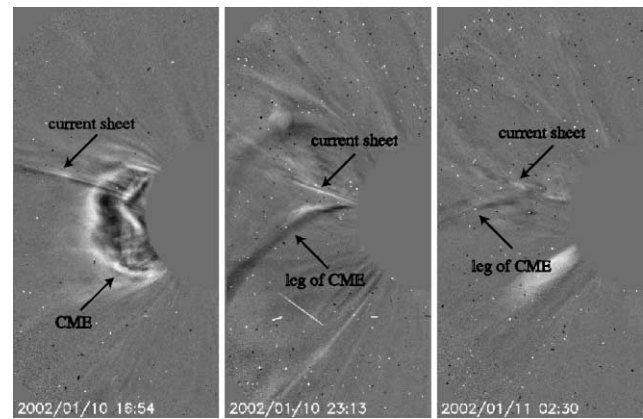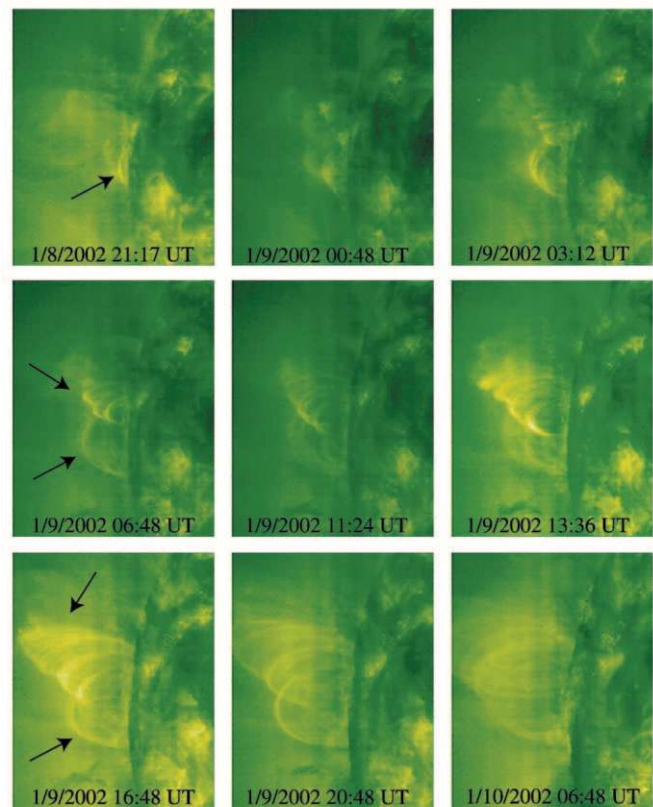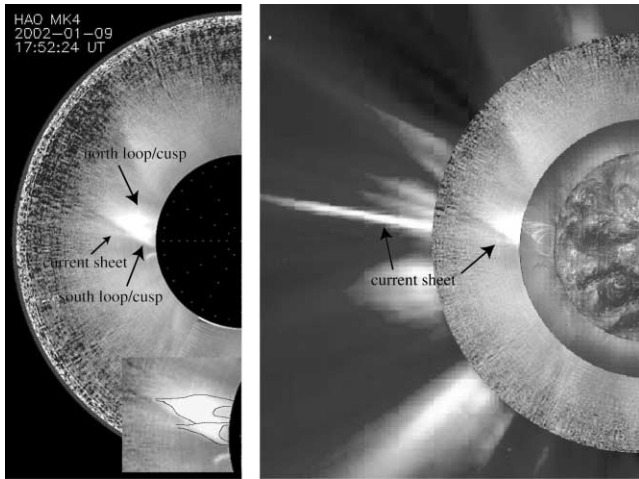Fig. 10.—*Left:* MLSO MK4 white-light image at 17:52 UT, January 9, showing two loop/cusp systems after the CME. The inset shows our perception of what the two loop/cusp systems might look like. *Right:* Composite of EIT 195 Å (at 17:36 UT), MK4 (at 17:52 UT), and LASCO C2 (at 17:54 UT) images of January 9 showing that the current sheet feature seen in C2 corresponds to the south loop system in MK4 and EIT. [*See the electronic edition of the Journal for a color version of this figure.*]

loops, we would expect them to be above the EUV loops (see § 1), which is consistent with Figure 11.

2.3. *High-Temperature Emission*

SOHO/UVCS observed this current sheet feature from 17:48 UT, January 10, to 03:47 UT, January 11. The data reported here were taken from the O VI channel. The slit width was set to 100 μm, which corresponds to an instantaneous FOV of $40' \times 28''$. The slit angle was at P.A. = 78° and a projected heliocentric height of 1.53 $R_\odot$. The data were obtained with a spatial binning of 10 pixels (70″) and a spectral binning of 2 pixels (0.198 Å). Using four grating positions, UVCS data have extended spectral coverage of
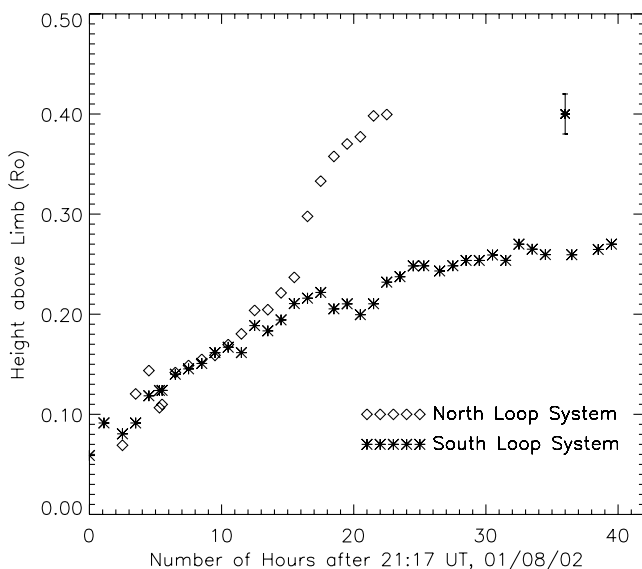

Fig. 11.—Height-time measurement of the two post-CME loop systems showing them rising above the limb. Since the position (longitude) of these loops should be within 1 day of the limb, the projection effect is small.

942.2–1097.7 Å for the O VI primary channel (471–549 Å in second order). Several other lines of interest can also be obtained from the O VI redundant channel. They are Lyα, Mg x λ609, [Fe XII] λ1242, N v λ1238, and [S x] λ1196. For a detailed description of the UVCS instruments, see Kohl et al. (1995). The raw data have been wavelength and flux calibrated. The uncertainty in the flux calibration is about 20% for the first-order lines (Gardner et al. 2000) and 50% for the second-order lines (Gardner et al. 2002). Stray light is negligible in the data, so no stray light correction is performed. Figure 12 plots the spatial distribution of several major lines and the intensity ratio of the O VI λ1032/λ1037 doublet (Fig. 12*j*). We separate the data into four spatial zones, which are indicated on the plots. Figure 13 plots the spatially averaged spectra for zones 2, 3, and 4 taken at one of the grating positions where we measure most of the line fluxes. We can see that zone 3 contains strong emission from highly ionized ions (such as [Fe XVIII] λ974 and [Ca XIV] λ943) that are rarely seen in the corona at this height. This high-temperature emission is concentrated around P.A. = 81°.3 ± 3°.7 (half of the FWHM), which is along the same direction as the thin current sheet feature seen in C2. Zone 2 contains enhanced emission from low-ionization ions such as [Fe x] λ1028 and [Si VIII] λ944. We suspect that it is related to the erupted prominence material in the leg of the CME (that occurred starting 12:06 UT, January 10, in C2 as mentioned before) just south of the current sheet (see Fig. 6, *lower right panel*, and Fig. 8). Zone 4 would contain material from the bright streamer north of the current sheet. Table 1 lists the line intensities for all four zones. In the following analysis of the UVCS data, we will concentrate on zones 2, 3, and 4 only. The fluxes measured for zone 1 are listed but are not relevant for the present study.

Figure 12*j* plots the O VI λ1032/λ1037 intensity ratio, which can be used as an indicator of the outflow speed of the ions because of the Doppler dimming effect (Hyder & Lites 1970; Noci, Kohl, & Withbroe 1987; Strachan et al. 2000). When the outflow is less than 100 km s^{-1}, the λ1032/λ1037 ratio is between 2 and 4 depending mainly on the outflow speed and the electron density (and weakly on the electron temperature)—the higher the speed or the larger the density, the smaller the ratio. When the outflow exceeds 100 km s^{-1}, the ratio goes below 2 because of the pumping of O VI λ1037.6 by C II λ1037.0 (Noci et al. 1987). Figure 12*j* shows that the ratios are larger than 2 in all four zones, which implies that the outflow speed is less than 100 km s^{-1}. Zone 3 has the lowest values of the ratio, which implies that either the electron density or the outflow speed (or the combined effect of the two) is the highest in zone 3. Since there are probably both current sheet and background corona (as in zone 4; see § 3.2) overlapping in the line of sight, it is possible that the outflow speed in the current sheet is higher than 100 km s^{-1} (which should give the O VI doublet ratio below 2) but the "average" O VI doublet ratio is still above 2 as integrated along the line of sight with most contribution from a much lower outflow speed in the background corona.

SOHO/CDS made observations from 07:00 to 15:30 UT on January 10. The observation sequence consists of six rasters (ARDIAG_2), each with FOV of $4' \times 4'$. Twenty spectral windows include a wide selection of transition region and coronal lines, providing temperature diagnostics as well as relative abundances of Fe, Si, Ca, Ne, Mg, and O. Figure 14 shows the images in Mg IX 368.07 Å (10^6 K
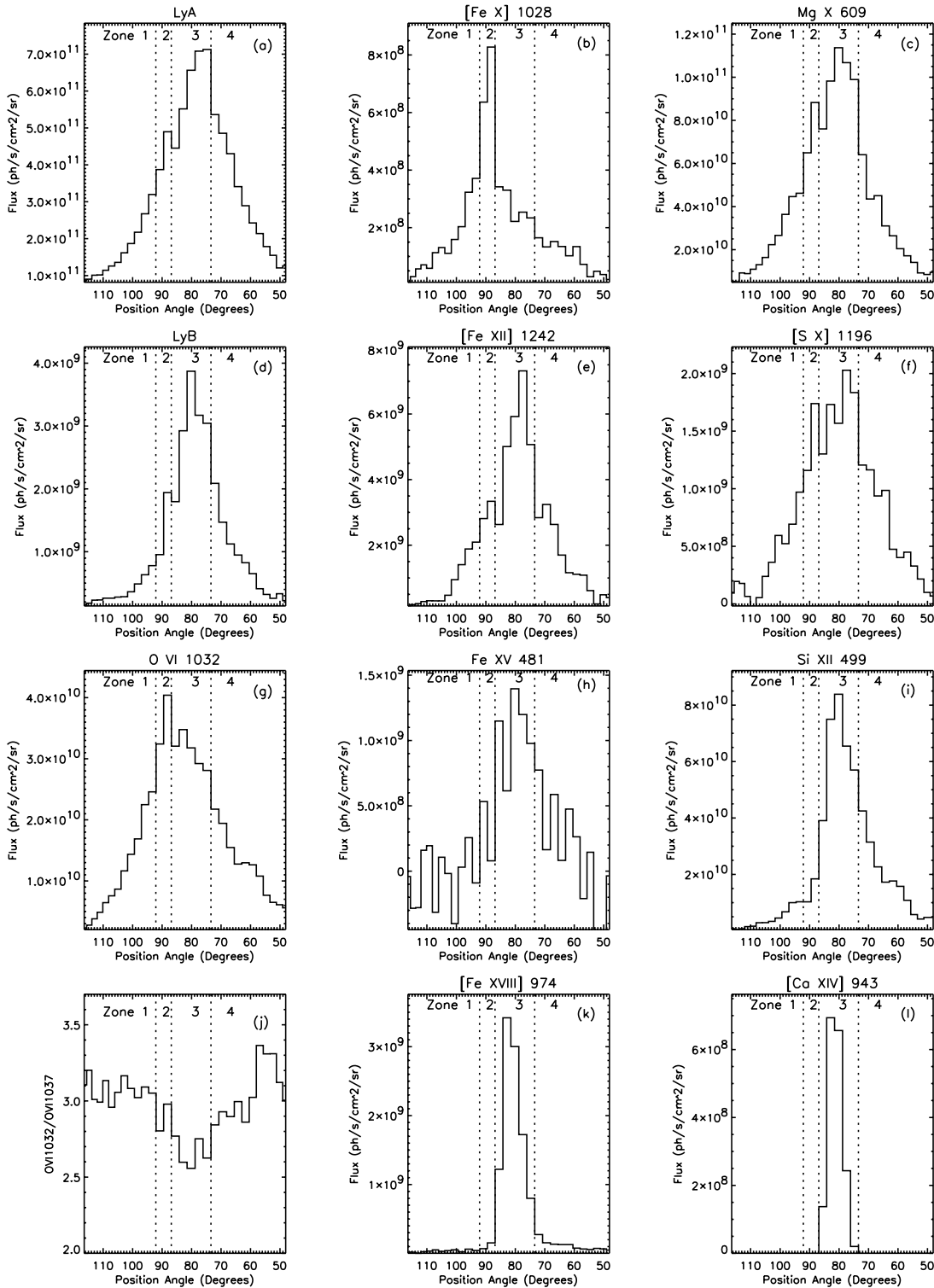
Fig. 12.—Spatial distribution of several major lines from UVCS data and the intensity ratio of the O vi $\lambda1032/\lambda1037$ doublet (Fig. 12*j*)

formation temperature) and Fe xvi 360.8 Å (2.5×10^6 K) composed from the six rasters. Both images show multiple loop structure extending up to the edge of the FOV. For example, the outer tip of the Mg ix loops appeared to be at around $X = -1400''$, $Y = +200''$, which corresponds to $\sim1.46\ R_\odot$ at P.A. $= 82°$. The Fe xvi loops appeared to be along the same direction but even higher up. This is consistent with the P.A. of the high-temperature emission

observed by UVCS (see Fig. 12). Even though these loops may be mixed with other parts of the active region, the outer boundary of the loops is probably associated with the post-CME reconnection loops like those seen by EIT (Fig. 9; also cf. Fig. 2). However, the two loop systems seen by EIT on January 9 were not clearly distinguishable in the CDS images that were taken on January 10. In fact, the two loop systems have also become too faint to be clearly
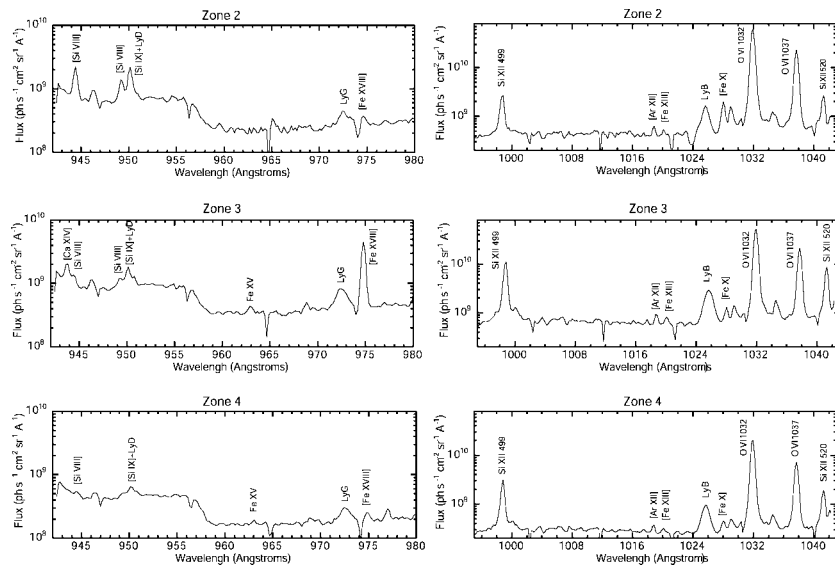
FIG. 13.—UVCS spectra for zones 2, 3, and 4 taken at grating position 236900, which covers the wavelength range of 942.2–1042.5 Å (471–521 Å in second order). Low-ionization lines ([Si VIII] λ944 and [Fe x] λ1028) are particularly strong in zone 2, and high-ionization lines ([Fe XVIII] λ974 and [Ca XIV] λ943) are particularly strong in zone 3.

distinguishable in EIT on January 10 (see bottom right panel of Fig. 9). In Figure 14, the lower edge of the Mg IX loops (probably associated with the south loop system) is plotted on both panels. It shows that the lower temperature emission loops (i.e., Mg IX) were located inside the higher temperature loops (Fe XVI). This is consistent with the expectation of the flare loop models (e.g., Forbes & Acton 1996; see § 1).

Figure 15 shows the MK4 image at 19:28 UT, January 10 (*left panel*), and the composite image from EIT 195 Å (19:36 UT), CDS Fe XVI, MK4 (19:28 UT), and C2 (20:26 UT) images (*right panel*; all on January 10). Superposed on the image at the right panel is the projection of the UVCS slit on the plane of the sky (note that the width is not to scale) showing the spatial distribution of the [Fe XVIII] λ974 emission. The two "loops" (see the inset in the left panel) and the current sheet feature (thin streamer) above the loops in the MK4 image seem to be still preserved at this time. However, it is less certain that the current sheet corresponds to the south loop system, probably because of the way the two

loops were projected in the plane of the sky. These loops seen by MK4 are probably unrelated to the bright streamer seen by C2 at the north of the current sheet because the size of the loops in MK4 is much less than that of the bright streamer in C2. We can see that the high-temperature emission seen by UVCS and CDS is along the same direction of the current sheet feature in MK4 and C2, as expected from the models, although the center of the high-temperature emission (seen by UVCS and CDS) is at P.A. $\sim 81°$ and that of the current sheet seen by C2 is at P.A. $\sim 78°$. This may be due to the fact that the field lines associated with the current sheet are nonradial, especially when it was disturbed by the CME earlier that day (see Fig. 8). Note that
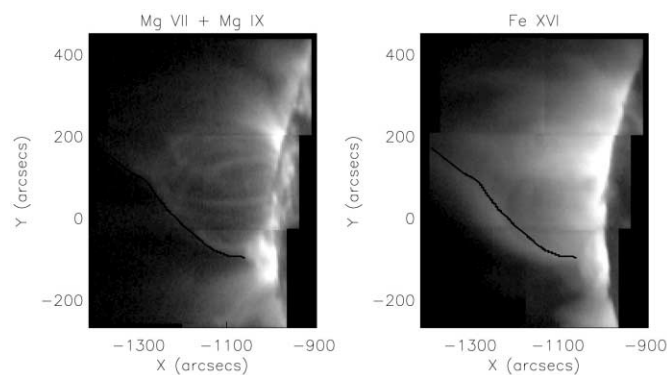

FIG. 14.—Images of Mg IX λ368.07 (formation temperature of $\sim 10^6$ K, with a small contribution of Mg VII λ367.68) and Fe XVI λ360.8 (formation temperature of $\sim 2.5 \times 10^6$ K) composed from six rasters of the CDS observations on January 10. The line marks the lower boundary of the Mg IX loops, which indicates that the Mg IX loops are inside the Fe XVI loops.
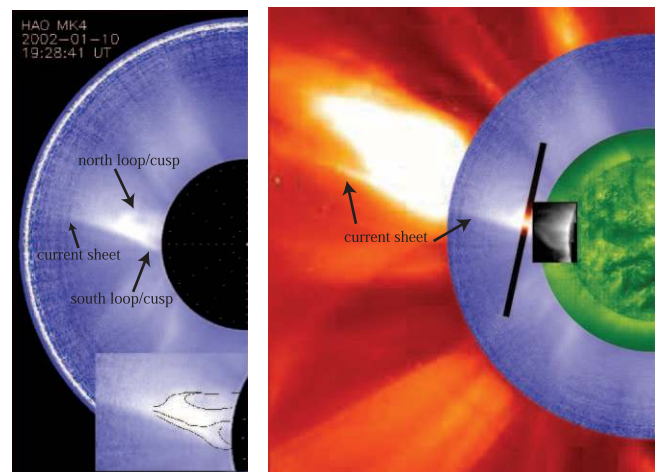
FIG. 15.—*Left:* MLSO MK4 white-light image at 19:28 UT, January 10, showing that the two loop/cusp systems still exist 2 days after the CME. The inset shows our perception of what the two loop/cusp systems might look like. *Right:* Composite image from EIT 195 Å (19:36 UT), CDS Fe XVI (small rectangle at the limb), MK4 (19:28 UT), and C2 (20:26 UT) images of January 10. Superposed on the image is the projection of the UVCS slit on the plane of the sky (the width is not to scale) showing the spatial distribution of the [Fe XVIII] λ974 emission (cf. Fig. 12k). It is clear that the high-temperature emission is along the direction of the current sheet.

TABLE 1
LINE INTENSITIES

λ_{ID} (Å)	Identification	Zone 1 ($\times10^7$ photons cm^{-2} s^{-1} sr^{-1})	Zone 2 ($\times10^7$ photons cm^{-2} s^{-1} sr^{-1})	Zone 3 ($\times10^7$ photons cm^{-2} s^{-1} sr^{-1})	Zone 4 ($\times10^7$ photons cm^{-2} s^{-1} sr^{-1})	Measurement Error (%)	Calibration Error[a]
481.45	Fe xv $3s3p\ ^1P_1$–$3p^2\ ^1D_2$	...	...	102.0	19.9	<20	2
609.79	Mg x $2s\ ^2S_{1/2}$–$2p\ ^2P_{3/2}$	1988.4	7414.3	9668.5	2634.0	<10	2
499.37	Si xii $2s\ ^2S_{1/2}$–$2p\ ^2P_{3/2}$	378.7	1488.2	6419.6	1580.5	<10	2
510.05	Fe xiii] $3s^23p^2\ ^3P_2$–$3s3p^3\ ^5S_2$	22.1	46.4	148.9	32.9	<20	2
520.66	Si xii $2s\ ^2S_{1/2}$–$2p\ ^2P_{1/2}$	116.1	649.6	2705.7	491.6	<10	2
943.61	[Ca xiv] $2p^3\ ^4S_{3/2}$–$2p^3\ ^2D_{3/2}$	...	...	45.3	...	<20	1
944.38	[Si viii] $2p^3\ ^4S_{3/2}$–$2p^3\ ^2P_{3/2}$	12.7	68.5	19.2	3.6	<20	1
949.22	[Si viii] $2p^3\ ^4S_{3/2}$–$2p^3\ ^2P_{1/2}$	7.6	39.9	12.0	...	<30	3
950.15	[Si ix] $2p^2\ ^3P_1$–$2p^2\ ^1S_0$, Lyδ	18.2	76.5	27.5	16.4	<20	3
972.54	Lyγ	...	...	54.2	13.8	<20	1
974.86	[Fe xviii] $2p^5\ ^2P_{3/2}$–$2p^5\ ^2P_{1/2}$	...	7.1	201.5	5.4	<10[b]	1
1018.60	[Ar xii] $2p^3\ ^4S_{3/2}$–$2p^3\ ^2D_{5/2}$	2.4	9.7	18.8	4.8	<10	1
1025.72	Lyβ	32.0	121.7	287.7	75.8	<10	1
1025.72	Lyβ collisional component	10.3	62.2	205.6	37.7	<10	1
1028.04	[Fe x] $3d^4D_{7/2}$–$3d^4F_{7/2}$	14.7	76.8	27.1	8.6	<10	1
1031.91	O vi $2s\ ^2S_{1/2}$–$2p\ ^2P_{3/2}$	1041.2	3597.9	3086.9	1176.1	<10	1
1031.91	O vi collisional component	331.9	1438.1	1598.7	417.1	<10	1
1037.61	O vi $2s\ ^2S_{1/2}$–$2p\ ^2P_{1/2}$	343.3	1259.0	1171.4	398.3	<10	1
1054.90	[Ar xii] $2p^3\ ^4S_{3/2}$–$2p^3\ ^2D_{3/2}$	...	...	21.1	4.5	<10	1
1196.25	[S x] $2p^3\ ^4S_{3/2}$–$2p^3\ ^2D_{5/2}$	37.2	156.6	176.7	54.8	<10	1
1215.67	Lyα	15785.5	43703.5	61149.5	28171.5	<10	1
1238.82	N v $2s\ ^2S_{1/2}$–$2p\ ^2P_{3/2}$	40.1	111.5	90.1	49.0	<20	1
1242.03	[Fe xii][c] $3p^3\ ^4S_{3/2}$–$3p^3\ ^2P_{3/2}$	64.9	308.9	540.8	122.9	<10	1

[a] 1 = first order (<20%); 2 = second order (~50%); 3 = blend.
[b] For zone 3 only; zones 2 and 4 have uncertainties of less than 30%.
[c] N v λ1242 has been subtracted using half of the N v λ1238 flux.

the high-temperature emission still exists even 2 days after the January 8 CME. We note that CDS data contain a wealth of spectral lines, which will enable us to derive physical properties (e.g., temperature and abundances) in the post-CME loops. Since in this paper we would like to concentrate on the properties of the current sheet above these loops, more detailed CDS data analysis will be deferred to a later study.

Since we expect the temperature to be high in both the current sheet and the closed loop region below the cusp (i.e., inside the lower tip of the current sheet; cf. Fig. 2), there is the question of which corresponds to the high-temperature emission observed by UVCS. The spatial extent of the [Fe XVIII] $\lambda 974$ emission is about $190''$ wide (FWHM). The width of the current sheet as seen in LASCO C2 on January 10 is about $2°$ (in P.A.) at 3.5 $R_\odot$, which corresponds to about $120''$ wide. These two widths are comparable but may imply a narrowing with height. The southern loop system seen in MK4 (Figs. 10 and 15) likely corresponds to the current sheet observed by C2 and the high-temperature emission observed by UVCS, and its "cusp" appears to be at around 1.5 $R_\odot$ (see the inset in the left panel of Fig. 15). It is thus difficult to tell from the morphological argument whether the UVCS slit was above the cusp (i.e., across the current sheet) or just below it. At this moment, we will assume that the high-temperature emission observed by UVCS comes from the current sheet. This assumption will gain further support by the abundance and emission measure analysis in § 3.2.

2.4. Source Region of the CME

Since we can clearly see the post-CME loops at the limb, it is certain that the source region of this eruption was very close to the limb at the onset of the event. Figure 16 shows the Big Bear Solar Observatory (BBSO) Hα[6] (22:32 UT of January 14; left panel) and EIT 304 (19:19 UT of January 15; right panel) images when the active region complex AR 9782/9785 was at the east part of the disk. Their position indicates that it was right at the limb on January 10. The latitude of AR 9782 is $9°$ above the equator, which is right around the direction of the current sheet. This indicates that the CME on January 8 is very likely to originate from this active region (also cf. Fig. 3). This is consistent with the observations that fast CMEs (speed >1000 km s^{-1}) are more likely to originate from active regions (Gosling et al. 1976; MacQueen & Fisher 1983; St. Cyr et al. 1999). There are two filaments at this active region complex. The lower one is in the east-west direction, and the upper one is in the north-south direction. The shape of these filaments is analogous to the motion of the two post-CME loop systems (cf. Fig. 9). Since filaments are well known to form along neutral lines (e.g., Smith & Ramsey 1967; Martin 1973) and so are the postflare/CME loops as well as the streamers, it is reasonable to speculate (because we did not actually observe it) that they may be related to the CME eruption and the position of the current sheet (which is above those post-CME loops). If this is the case, it explains why this current sheet (which corresponds to the south loop system) stands out in this observation—it was oriented almost edge-on (assuming it is associated with the east-westward filament) so we
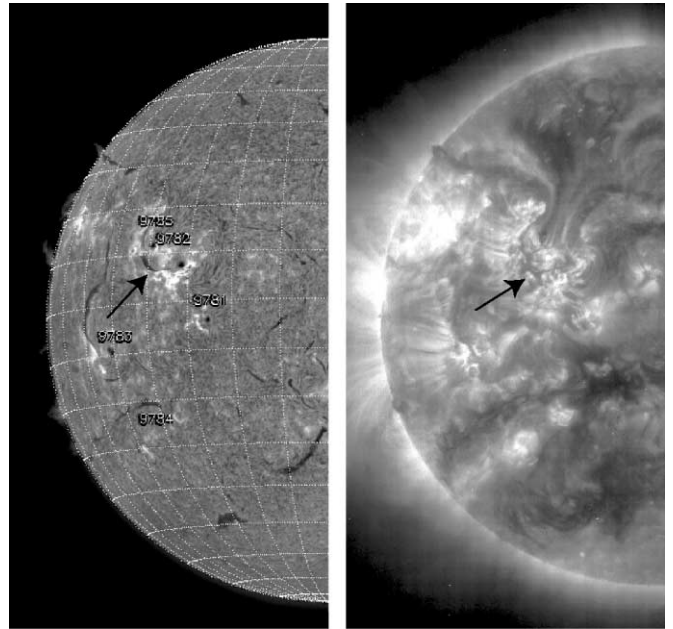
---

[6] The image in the left panel of Fig. 16 was downloaded from the BBSO Active Region Monitor web site at http://www.bbso.njit.edu/arm.

Fig. 16.—BBSO Hα (left; 22:32 UT, January 14) and EIT 304 (right; 19:19 UT, January 15) images when the active region complex AR 9782/9785 (indicated by the arrow) was at the northeast part of the disk. This region is likely the source region of the January 8 CME.

were looking through the sheet along the line of sight, maximizing the emission measure and thus its brightness.

3. PROPERTIES OF THE CURRENT SHEET

In the previous section, we described the observations of a CME, the post-CME loops, and the current sheet. They agree well with the general picture expected from the CME/flare-loop models as described in § 1. In this section, we concentrate on this current sheet feature, which was left by the CME and remained for more than 2 days. We discuss the dynamical properties of the current sheet and the physical properties (electron temperature, electron density, emission measure, and elemental abundances) in the current sheet material. We then interpret the observations based on the model by LF00 and Lin02, whose predictions of the CME and current sheet properties agree with many aspects of the observations.

3.1. Dynamics

Figure 17 is the LASCO C2 limb synoptic maps (LSMs; Li, Jewitt, & LaBonte 2000) showing the movement of the current sheet along position angle with time. These LSMs are constructed by summing over the C2 white-light signals from 3.0 to 3.5 $R_\odot$ (Fig. 17, upper panel) and from 5.0 to 5.5 $R_\odot$ (Fig. 17, lower panel) for each time sequence of C2 images. The long vertical stripes indicate CMEs. We can see that the current sheet initially moves northward more rapidly as it gradually slows down on January 10 at P.A. $\sim 78°$. The variation in P.A., especially the equator crossing in the early phase, cannot be totally accounted for by the projection effect as the Sun rotates. Therefore, it should be related to the self-adjustment of the magnetic structure after the CME. One possibility is that the CME displaced the background field to the south, and as the current sheet eliminates
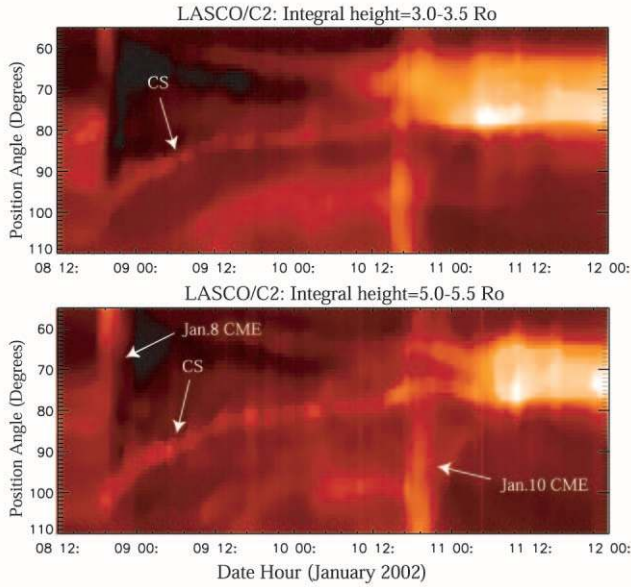
FIG. 17.—LASCO C2 limb synoptic maps at (*top*) 3.0–3.5 $R_\odot$ and (*bottom*) 5.0–5.5 $R_\odot$ showing the latitudinal movement of the current sheet with time. The current sheet moves about 20° in latitude in the course of 1 day. The CME on January 10 seems to temporarily push the current sheet farther northward. These maps also show the appearance of the bright streamer at the limb north of the current sheet on January 10 (cf. Fig. 4).

the field within the CME, the background field pushes back to its original position. The current sheet moves about 20° in latitude (and seems to go back to where the CME source region is) in the course of 1 day. This timescale should be naturally related to that of the field self-adjustment. Note that the current sheet appears to be two channels of outflowing blobs within a few hours after the CME (see Fig. 5), and they combine into one later on January 9, at least when seen in the plane of the sky. Reasons for this may include the geometry and topology of the current sheet, local density fluctuations, integration effects, and viewing angle.

We have measured the height versus time for about 10 transient bright features (i.e., blobs; see examples in Fig. 7) as they moved along the current sheet. Most of them have nearly constant speed, and a few others exhibit acceleration. Figure 18 shows two examples of the height-time measurements from two blobs in the current sheet. One shows constant speed at 586 km s^{-1} (Fig. 18, *right panels*), and the other (Fig. 18, *left panels*) shows tangential speed of 140–550 km s^{-1} with acceleration of about 60 m s^{-2}. Other blobs have speeds ranging from 300 to 650 km s^{-1}, some with small acceleration (below 100 m s^{-2}). These speeds are presumably close to the local Alfvén speed in the current sheet when the reconnection occurs (see § 1).

3.2. *Temperature, Density, and Abundances*

UVCS data contain emission lines from ions of several elements, including hydrogen, as well as ions from several ionization stages of Fe and Si. This allows us to derive the emission measure distribution as a function of the electron temperature, as well as the absolute abundances (i.e., abundance relative to hydrogen). In coronal conditions, the electron density is low enough that the lines are produced by electron collisional excitation followed by spontaneous emission. The line intensity is thus

$$I_{\text{line}} = \frac{1}{4\pi}\frac{n_{\text{el}}}{n_{\text{H}}}\int G(T_e)\,d\text{EM}(T_e)\ \text{photons cm}^{-2}\ \text{s}^{-1}\ \text{sr}^{-1}\ ,$$

(1)

where $n_{\text{el}}/n_{\text{H}}$ is the elemental abundance relative to hydrogen (i.e., absolute abundance); $G(T_e)$ is the contribution function, which is defined as

$$G(T_e) = \frac{n_{\text{ion}}}{n_{\text{el}}}(T_e)B_{\text{line}}q_{\text{line}}(T_e)\ ,$$

(2)

where $n_{\text{ion}}/n_{\text{el}}(T_e)$ is the ionic fraction, which is a function of the electron temperature T_e, B_{line} is the branching ratio for the line transition, and $q_{\text{line}}(T_e)$ is the electron excitation rate, which is a function of only the electron temperature in the low-density limit; and $d\text{EM}(T_e) = n_e n_{\text{H}}\,dl$ is the emission measure (in cm^{-5}) at a given electron temperature. The atomic rates are mostly adopted from the CHIANTI database version 4.01 (Dere et al. 1997; Young et al. 2003), except for the hydrogen Lyman series and [Fe XII] $\lambda1242$ rates (see Ko et al. 2002 for details). The ionization equilibria of Mazzotta et al. (1998) are adopted. In principle, the general shape of EM(T_e) is constrained by lines of the same element (Si and Fe), and the absolute abundances are constrained by the line fluxes relative to Lyβ.

We find that zone 4 can be approximated as isothermal with electron temperature around 1.6×10^6 K and that the absolute abundances show a strong first ionization potential (FIP) effect. The isothermal nature of the emitting region, the temperature, and the FIP effect are all quite similar to the properties of streamers reported by Raymond et al. (1997) and Feldman et al. (1998) as determined by similar methods. Zones 2 and 3 should contain the same loop system in the line of sight but with different amounts of material depending on what part of the loop system falls within the FOV. We therefore assume that zones 2 and 3 contain isothermal components at 1.6×10^6 K and the elemental abundances found for zone 4, with only the emission measure being scaled.

Zone 3 shows higher temperature emission, in particular the [Fe XVIII] and [Ca XIV] lines. We add a high-temperature component to match these lines. We first choose the emission measure of the isothermal component by matching the line fluxes for the lower ionization lines, which have no contribution from the high-temperature component. The emission measure of the hot component is chosen so that the total fluxes in the Lyman lines from the hot and isothermal components match those observed. Given the emission measure, absolute abundances can be determined. The hot component makes no significant contribution to the intensities of lines of high-FIP elements, so unfortunately we have little information about the high-FIP elements. We expect that the Ca and Fe abundances ought to scale together because both are low-FIP elements, but some scatter is observed in Ca-to-Fe ratios (e.g., Fig. 2 of Raymond 1999), perhaps related to the very low FIP of calcium. For the high-temperature component, a single temperature that matches the [Ca XIV] intensity within a reasonable abundance range does not quite account for the [Fe XVIII] intensity or for the Si XII and Fe XV emission beyond that predicted by the isothermal component. A similar situation occurs for a single temperature that
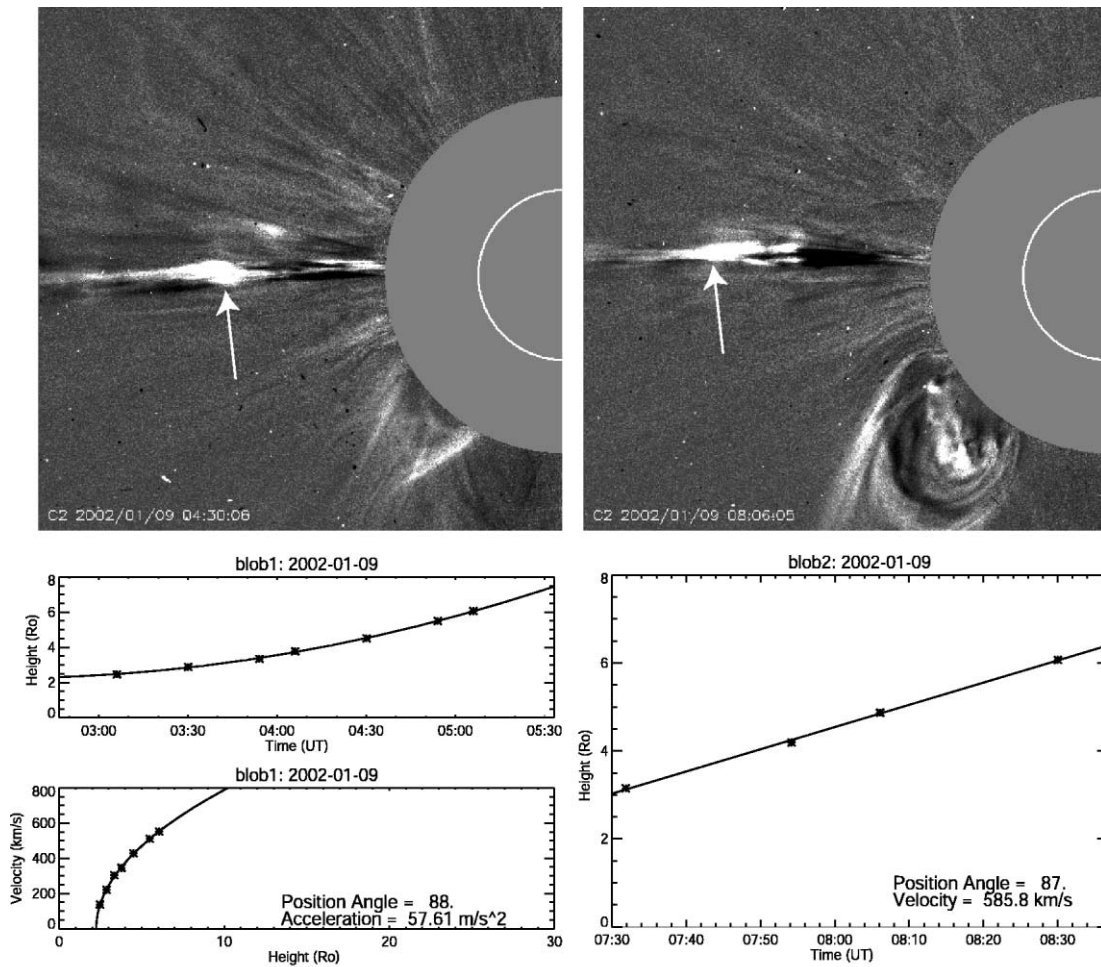
Fig. 18.—Two examples of the height-time measurements of the blobs in LASCO C2 showing acceleration (*left*) or constant speed (*right*). The bottom left panel shows the speed evaluated as tangents at points on the height-time plot (*middle left*). The upper two panels are the LASCO C2 running difference images at 04:30 UT, January 9 (*left*), and 08:06 UT, January 9 (*right*), showing one of the blobs (indicated by the arrow) corresponding to these height-time measurements.

matches the [Fe xviii] intensity. Therefore, we spread the high-temperature component over a modest range of temperature.

Similarly, we must add a low-temperature component to zone 2. The isothermal component is determined to match the higher ionization lines such as Si xii and [Fe xiii]. The total low-temperature emission is constrained by the requirement that the sum of isothermal and low-temperature components match the Lyman line fluxes. The temperature is chosen to match the lowest temperature emission lines, such as [Si viii] and [Fe x], with the constraint that the total emission from the low-temperature and isothermal components for lines such as O vi, [Si ix], and N v must match the observations. As for the hot component in zone 3, the fit is somewhat improved if the low-temperature component is spread over a modest temperature range. The uncertainty is larger in this case since both components contribute nonnegligibly to the emission of most lines, with different degrees for different lines.

Overall, while the detailed shapes of the emission measure distributions within the low- and high- temperature components in zones 2 and 3 are not well determined, the total emission measures and the elemental abundances should be reliable. We also note that faint [Fe xviii] emission is present

in zones 2 and 4 but that no other high-temperature lines are detected. The lack of other emission lines makes it impossible to characterize this emission component, except that the emission measure is small enough that it makes no significant contribution to the other emission lines we analyze.

Figure 19 shows the emission measure distribution that matches the UVCS line intensities for the three zones (Fig. 19*a*), the absolute abundances (Fig. 19*b*), and the fitting results of these lines (Fig. 19*c*). The absolute abundances shown are relative to their photospheric values (Allen 1973). The high T_e component in zone 3 is around $(3-4) \times 10^6$ K, and the low-T_e component in zone 2 is around 10^6 K. All three zones show the FIP effect. The high-T_e component of zone 3 mainly constrains the abundances of Ca and Fe, and they have similar abundances to those in zone 4 (note that we are able to obtain a satisfactory fit using the same abundances in both zones 3 and 4 except the Ca abundance, which is constrained only by the high-T_e component of zone 3). This implies that the current sheet consists of material having the same origin as the bright streamer north of it. The absolute abundances in zones 3 and 4 show not only the FIP effect but also that, while the low-FIP elements are enhanced by a factor of 2–3 above their photospheric values, the high-FIP elements are depleted by a factor of
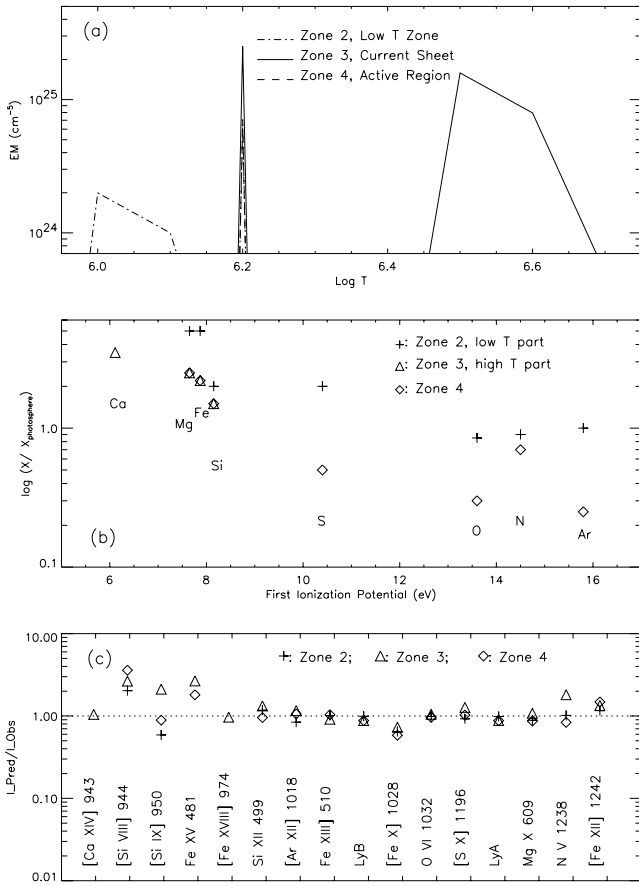
FIG. 19.—(a) Emission measure distribution that matches the UVCS line intensities for the three zones, (b) absolute abundances, and (c) fitting results. All three zones have an isothermal component at 1.6×10^6 K. Zone 2 has an additional low-temperature component at around 10^6 K. Zone 3 has an additional high-temperature component at $(3–4) \times 10^6$ K. See text for details.

about 2–3. Previous measurements (e.g., Raymond et al. 1997; Ko et al. 2002) have found similar abundance properties for active region streamers, and the absolute abundances are found to decrease with height, partly because of gravitational settling (Lenz, Lou, & Rosner 1998; Raymond 1999; Ko et al. 2002). The absolute abundances in the flare loops are found to be closer to photospheric (e.g., about a factor of 2 or lower enhancement for the low-FIP elements as observed by Sylwester et al. 1998 and Fludra & Schmelz 1999). Indeed, we would expect the abundances in these postflare/CME loops (i.e., inside the cusp) to be closer to photospheric because of chromospheric evaporation (see § 1) that brings material deeper down in the photosphere/chromosphere up to the corona. Therefore, the strong FIP effect in zone 3 with enhancement of the low-FIP elements and depletion of the high-FIP elements relative to their photospheric values supports the picture that the UVCS slit was above the cusp (i.e., across the current sheet) and that the material inside the current sheet is brought in from the sides of the sheet, i.e., from the ambient corona (Yokoyama et al. 2001). It is interesting to note that zone 2 not only shows a weaker FIP effect but also that the absolute abundances are systematically higher than those in zones 3 and 4 for both low- and high-FIP elements. As mentioned above, the low-T_e component in zone 2 is probably associated with the erupted prominence later on January 10 and thus has a dif-

ferent origin of material from those in the current sheet structure and the streamer. Note that this type of emission measure analysis is subjective and the " good-fit " results for the emission measure distribution and the abundances often are not unique (see, e.g., Del Zanna, Bromage, & Mason 2001). However, we are confident that the results shown here correctly represent these regions in general.

Ciaravella et al. (2002) observed a post-CME current sheet feature that also exhibits high-temperature emission such as [Fe XVIII] λ974, [Ca XIV] λ943, and Fe XVII λ1153. Their analysis shows that the electron temperature inside the current sheet is around $(4–6) \times 10^6$ K and the emission measure is around 10^{25} cm^{-5} at 1.50 $R_\odot$, which is similar to our case here. The absolute abundances in their study also show the FIP effect, but their values are about a factor of 2 larger than those in our case for both the low- and high-FIP elements. It is interesting to note that Ciaravella et al. (2002) also observed a simultaneous presence of cool gas (enhanced [Si VIII] λ944 and [Fe X] λ1028 emission) next to the hot [Fe XVIII] λ974 emission.

If we assume that the depth of the current sheet along the line of sight is at least the same as the width in the plane of the sky ($\sim$190″), the emission measure for the high-T_e part of zone 3 ($\sim$$2 \times 10^{25}$ cm^{-5}) implies an upper limit of the electron density of $\sim$$4 \times 10^7$ cm^{-3} at 1.53 $R_\odot$. This is much lower than what is observed (and expected by the flare models) in the X-ray flare loops (e.g., Withbroe 1978; see § 1). This supports the assumption that the UVCS slit was across the current sheet (i.e., above the cusp), where the density is expected to be comparable to the ambient corona. We can also use the LASCO C2 data to estimate the electron density inside the current sheet at a given height. We select a blob as seen from the LASCO C2 image at 4.4 $R_\odot$, 04:30 UT of January 9 (Fig. 18, left panel). Assuming the measured brightness is from Thomson scattering off the coronal electrons, we use the equations of Billings (1966, p. 65) to calculate the total electron content. Assuming the thickness along the line of sight is the same as the width of the blob in the plane of the sky ($\sim$340″ in this case; note that the width of this blob is larger than that of the current sheet outside of the blob, which is about half as wide), we obtain an electron density of 3.4×10^6 cm^{-3} in the blob. Assuming the same line-of-sight thickness for comparison purposes, we obtain an electron density of 2.3×10^6 cm^{-3} in the current sheet outside of the blob and 3.1×10^5 cm^{-3} in the corona just outside and south of the current sheet. A measurement of another blob at 07:31 UT, January 9 (at 3.0 $R_\odot$; see right panel of Fig. 18), gives an electron density of 4.0×10^6 cm^{-3} in the blob.

We note that the electron density found at 1.53 $R_\odot$ is about an order of magnitude higher than that found above 3 $R_\odot$. As the plasma gains kinetic energy following the reconnection, part of the bulk material flows outward along the current sheet. It naturally expands because of decreasing pressure in the corona surrounding the current sheet; therefore, the density decreases. At the same time, however, reconnection can occur continuously inside the current sheet as the plasma flows along, thus continuing to boost the energy of the outflowing plasma. This continuous energy input may help maintain the flow of the plasma (e.g., blobs) as it flows out against the gravitational field of the Sun.

We also note that the radiative component of O VI λ1032 (which is proportional to the electron density n_e times a

Doppler dimming factor) in zone 3 is 1.96 times larger than that in zone 4, and the collisional component (which is proportional to n_e^2) is 3.83 times larger (see Table 1). This suggests that n_e is twice as high in zone 3 as in zone 4 and the Doppler dimming factors are the same. This also implies that the filling factor of the O VI gas in zone 3 is close to 1. This is reasonable since the contribution of the O VI emission from the high-T_e component of zone 3 is small. It is further supported by the fact that the emission measure of the isothermal component in zone 3 is about 4 times larger than that in zone 4 (see Fig. 19). Therefore, the lower O VI $\lambda 1032/\lambda 1037$ intensity ratio (Fig. 12j and Table 1) in zone 3 is almost entirely due to higher electron density, and the outflow speed in both zones should be below about 50 km s^{-1}. Note that most of the O VI emission does not come from the same plasma containing the [Fe XVIII] $\lambda 974$ emission (i.e., the high-T_e component), so this low speed does not necessarily apply to the current sheet. As discussed in § 2.3, even if there is substantial outflow inside the current sheet, it will be masked by the O VI emission in the background corona, which has low outflow speed. On the other hand, the contrasts of the radiative and collisional components between zone 2 and zone 4 are 2.85 and 3.45, respectively. This suggests that n_e is only about 20% larger in zone 2 than that in zone 4 and much of the enhancement of the O VI emission results from higher O abundance in zone 2, consistent with our abundance analysis (see Fig. 19).

3.3. Interpretation

The high temperature and dynamic nature of this thin streamer (i.e., the current sheet) formed behind a fast CME, along with the appearance of the post-CME loops, can be explained as the product of the reconnection processes associated with the CME eruption as outlined in § 1. The phenomena we report in this paper should be commonly associated with energetic eruptions from active regions. With the advantages of being a limb event and probably the special orientation (nearly edge on) of the current sheet, this particular event can provide good observational constraints for modeling the processes of the CME eruption.

The event investigated in this paper can find its theoretical counterpart from the work by LF00, Forbes & Lin (2000), and Lin02 on the basis of the catastrophic models of solar eruptions. In these models, the loss of mechanical equilibrium in a magnetic system quickly expels the magnetic flux rope, which is usually used to model the current-carrying prominences or filaments. A current sheet forms behind the flux rope with the magnetic field being stretched out by the eruption. As schematically described by Figure 2, magnetic dissipation or reconnection occurring in the current sheet converts the magnetic energy to the thermal and kinetic energy. This also allows the flux rope to escape smoothly to form a CME (Fig. 2, *upper part*) and creates separating flare ribbons on the solar disk and successively rising postflare/CME loops/giant arches in the corona (Fig. 2, *lower part*). Because the 2002 January 8 event occurred just behind the limb, the data we obtained cannot provide us with precise information about the flare ribbons, but the loop system continuously moving upward does constitute evidence that the magnetic reconnection is occurring or has occurred according to the standard two-ribbon flare models (e.g., Kopp & Pneuman 1976; Schmieder et al. 1987; Lin et al. 1995; and Forbes & Acton 1996).

In the context of mass ejections, LF00 showed that fast magnetic reconnection is essential for a catastrophe, which is basically an ideal-MHD process, to develop into a plausible eruption. If the magnetic reconnection does not occur or occurs too slowly, the current sheet cannot be eroded efficiently, and magnetic tension force produced by the magnetic field lines that pass over the flux rope may prevent the flux rope from escaping. The whole process including the flare depicted by the lower part of Figure 2 will finally be halted. Fortunately, a major eruption does not require very fast reconnection. Even a fairly low reconnection rate, which is measured by the Alfvén Mach number M_A for the inflow into the reconnection site, is sufficient to dissipate the current sheet quickly enough to allow the flux rope to escape and the catastrophe to develop to an eruption. Here the Alfvén Mach number M_A is the velocity of the magnetic flux and the plasma flowing into the reconnection site in units of the local Alfvén speed. In an isothermal corona, LF00 found that M_A can be as small as 0.005 and still allow the flux rope escape. In a more realistic coronal density model given by Sittler & Guhathakurta (1999, hereafter SG99), this critical value of M_A should be slightly larger, up to $M_A = 0.013$. The best fit to the observations is obtained by assuming an inflow rate on the order of $M_A = 0.1$.

We note that the northward motion of the current sheet, roughly 20° in 1 day, corresponds to about 10 km s^{-1}. This is about 0.015–0.03 times the outflow speeds in the streamer, which we identified with the Alfvén speed. The northward motion should be related to the relaxation of the large-scale magnetic field and therefore to the inflow rate into the current sheet. Thus, the northward motion of the current sheet is in harmony with the parameters derived in Lin02.

Lin02 showed that the difference in the energetics and kinetic behaviors of the flux rope propagating in the different atmospheres is significant. For a background field of moderate strength, say, 100 G, the flux rope can be accelerated from tens of km s^{-1} up to more than 1000 km s^{-1} within about 10 minutes after the onset of the eruption with an average acceleration of more than 1 km s^{-2}. This can be compared to the CME in this paper, in which the acceleration is about 1 km s^{-2} within as early as 20 minutes after the eruption (see Fig. 4 and discussions in § 2.1). A similar range of high acceleration rates in the low corona within a short time of CME eruptions was also observed by, e.g., Zhang et al. (2001) and Alexander et al. (2002). This implies that the catastrophic loss of equilibrium in a magnetic system can quite efficiently accelerate a CME. However, the dynamic behavior of the current sheet manifests quite different patterns in different media.

In an isothermal environment, the local Alfvén speed increases with the height at large altitudes, which allows the rate of dissipation of the current sheet through the reconnection to increase with the height as well. This directly results in quick erosion of the current sheet and fast rising of the lower tip of the current sheet (refer to Fig. 7b of LF00 and Figs. 5f, 5g, and 5h of Lin02), which is the top of the postflare/CME loop system according to the standard reconnection model. We then expect a fairly high loop/arch system and well separated flare ribbons (Fig. 2, *lower part*). However, neither previous observations (Švestka 1996 and references therein) nor recent ones (Ciaravella et al. 2002), including the present work, seem to support this scenario. The evidence from these observations indicates that the heights of postflare/CME loops/giant arches are generally

lower than 0.6 $R_\odot$ above the surface, that a long current sheet exists for a long time, and that the lower tip of the current sheet can never be seen to rise over the inner edge of the LASCO C2 FOV, which is located at around 2.2 $R_\odot$.

In the more realistic SG99 model, on the other hand, the local Alfvén speed decreases with height, and so does the rate of magnetic reconnection. In this case, the erosion of the current sheet does not occur as fast as in the isothermal case, although the rate of magnetic reconnection can still allow an eruption (refer to Figs. 6a, 6b, and 6c of Lin02). Therefore, a fairly long current sheet should be left behind the CME, and the lower tip of the current sheet remains at small heights (see Figs. 6f, 6g, and 6h of Lin02). Comparing this result with the plot shown in Figure 11 explains why, in reality, the postflare/CME loop/giant arch system can hardly rise to very large altitudes and the lower tip is always below the edge of the LASCO C2 FOV. Comprehensively, the above discussions solidly suggest that an eruption (as in this event) demonstrating fast mass and magnetic flux ejection, as well as flaring activity, is very likely to result from the catastrophic loss of equilibrium in a coronal magnetic field followed by magnetic reconnection.

Since the UVCS slit (at 1.53 $R_\odot$) was probably above the cusp (i.e., across the current sheet), we can estimate the magnetic field strength in the corona when it underwent reconnection. For this purpose, it is reasonable to assume that the magnetic energy is equally converted to the kinetic energy and the thermal energy, although other nonthermal processes may also carry the energy away. Adopting an electron density of 4×10^7 cm^{-3} (upper limit) and electron temperature of 3×10^6 K at 1.53 $R_\odot$, we obtain a magnetic field strength B of 1.2 G. We can also use the kinetic energy measured by LASCO C2 to estimate B. Using the two measurements of the blobs, one at 4.5 $R_\odot$ (at 04:30 UT, January 9, $n_e = 3.4 \times 10^6$ cm^{-3}, $v = 428$ km s^{-1}; see Fig. 18, *left panels*) and the other at 3.1 $R_\odot$ (at 07:32 UT, January 9, $n_e = 4 \times 10^6$ cm^{-3}, $v = 586$ km s^{-1}; see Fig. 18, *right panels*), we obtain $B \sim 0.47$ and 0.69 G, respectively.

4. SUMMARY

We summarize our analysis as follows.

1. Thin threads of streamers showing continuous and transient outflows were formed behind a fast CME off the east limb on 2002 January 8. Post-CME loops were formed subsequently above the disk, which also grew in height. Both the streamer-like structures and the loops lasted for about 2 days. AR 9782/9785 is likely the source region of this CME. We interpret the thin streamer as the current sheet formed behind the CME based on the model by LF00 and Lin02. Kinetic energy converted from magnetic energy due to reconnection produces outflows along the current sheet. At the lower end of the current sheet is the upper tip of the reconnection loops, which would be seen as X-ray cusps. The loops observed by MK4 seem to be the white-

light counterpart of the X-ray cusps due to high density inside. These post-CME loops showed behaviors of both postflare loops and soft X-ray giant arches as defined by Švestka (1996).

2. The leading edge of the CME is found to have a constant acceleration rate of 0.19 km s^{-2} above 2.76 $R_\odot$. There is strong evidence that it went through much larger acceleration (~ 1 km s^{-2}) below this height.

3. We have analyzed the dynamical and physical properties of the current sheet feature. The blobs seen constantly flowing along the current sheet show cases of both constant speed and acceleration. This current sheet feature moves northward by about 20° in latitude in the course of 1 day, corresponding to about 10 km s^{-1}. This is about 0.015-0.03 times the outflow speeds in the streamer, which we identified with the Alfvén speed, i.e., $M_A \sim 0.015$–0.03.

4. High-temperature emission of $(3$–$4) \times 10^6$ K was seen by UVCS (at 1.53 $R_\odot$) along the direction of the current sheet, as well as the high-temperature (presumably post-CME) loops seen by CDS. The high-temperature gas seen by UVCS can be either inside the current sheet or inside the reconnection cusp. Our analysis indicates that the UVCS slit was across the current sheet, i.e., above the cusp. This high-temperature gas was produced by the conversion of part of the magnetic energy into thermal energy due to reconnection. The abundances in the high-temperature component (i.e., the current sheet) exhibit strong FIP effect, which is similar to that in the bright streamer north of it. This is consistent with the picture that the material inside the current sheet is brought in from the side of the sheet, i.e., from the ambient corona. The absolute abundances of the low-FIP elements are found to be enhanced, while those of the high-FIP elements are depleted, relative to their photospheric values. These values are similar to those found in some active region streamers.

5. We use the electron density, electron temperature, and outflow speed to estimate the magnetic field strength in the corona just outside of the current sheet. It is of the order of 1 G.

6. Even though the formation of the current sheet with reconnection cusp/loops should be a common feature of energetic CMEs erupted from active regions, this event stands out because of being a limb event and probably the edge-on orientation of the current sheet. Our analysis can provide a good observational constraint on models of CME eruption. We discussed one plausible model by LF00 and Lin02, whose prediction of the CME, post-CME loops, and current sheet properties agrees with many aspects of this observation.

REFERENCES

Acton, L. W., et al. 1992, PASJ, 44, L71
Akmal, A., Raymond, J. C., Vourlidas, A., Thompson, B., Ciaravella, A., Ko, Y.-K., Uzzo, M., & Wu, R. 2001, ApJ, 553, 922
Alexander, D., Metcalf, T. R., & Nitta, N. V. 2002, Geophys. Res. Lett., 29(10), 41-1
Allen, C. W. 1973, Astrophysical Quantities (London: Athlone)
Amari, T., Luciani, J. F., Mikić, Z., & Linker, J. 2000, ApJ, 529, L49

Antiochos, S. K., DeLuca, E. E., Golub, L., & McMullen, R. A. 2000, ApJ, 542, L151
Antiochos, S. K., DeVore, C. R., & Klimchuk, J. A. 1999, ApJ, 510, 485
Bentley, R. D., Doschek, G. A., Simnett, G. M., Rilee, M. L., Mariska, J. T., Culhane, J. L., Kosugi, T., & Watanabe, T. 1994, ApJ, 421, L55
Billings, D. E. 1966, A Guide to the Solar Corona (New York: Academic)
Brueckner, G. E., et al. 1995, Sol. Phys., 162, 357

Burkepile, J. T., Darnell, J. A., & De Toma, G. 2002, Eos, 83(47), Meeting suppl., Abs. SH61A-0431
Carmichael, H. 1964, in Physics of Solar Flares, ed. W. N. Hess (NASA SP-50; Washington: NASA), 451
Chen, J. 1996, J. Geophys. Res., 101, 27,499
Ciaravella, A., Raymond, J. C., Li, J., Reiser, P.,Gardner, L. D., Ko, Y.-K., & Fineschi, S. 2002, ApJ, 575, 1116
Ciaravella, A., et al. 2000, ApJ, 529, 575
Delaboudinière, J.-P., et al. 1995, Sol. Phys., 162, 291
Del Zanna, G., Bromage, B. J. I., & Mason, H. E. 2001, in AIP Conf. Proc. 598, Solar and Galactic Composition, ed. R. F. Wimmer-Schweingruber (Melville: AIP), 59
Démoulin, P., Hénoux, J. C., Priest, E. R., & Mandrini, C. H. 1996, A&A, 308, 643
Dere, K. P., Landi, E., Mason, H. E., Monsignori-Fossi, B. F., & Young, P. R. 1997, A&AS, 125, 149
Doschek, G. A., Strong, K. T., & Tusneta, S. 1995, ApJ, 440, 370
Feldman, U., Schüle, U., Widing, K. G., & Laming, J. M. 1998, ApJ, 505, 999
Fludra, A., & Schmelz, J. T. 1999, A&A, 348, 286
Forbes, T. G. 2000, Philos. Trans. R. Soc. London, A, 358, 711
Forbes, T. G., & Acton, L. W. 1996, ApJ, 459, 330
Forbes, T. G., & Isenberg, P. A. 1991, ApJ, 373, 294
Forbes, T. G., & Lin, J. 2000, J. Atmos. Sol.-Terr. Phys., 62, 1499
Forbes, T. G., Malherbe, J. M., & Priest, E. R. 1989, Sol. Phys., 120, 285
Forbes, T. G., & Priest, E. R. 1995, ApJ, 446, 377
Furth, H. P., Killen, J., & Rosenbluth, M. N. 1963, Phys. Fluids, 6, 459
Galeev, A. A., & Zelenyi, L. M. 1975, J. Exp. Theor. Phys. Lett., 22, 170
Gardner, L. D., Atkins, N., Fineschi, S., Smith, P. L., Kohl, J. L., Maccari, L., & Romoli, M. 2000, Proc. SPIE, 4139, 362
Gardner, L. D., et al. 2002, in The Radiometric Calibration of SOHO, ed. A. Pauluhn (ESA SR-002; ESA: Noordwijk), 161
Goldstein, R., Newgebauer, M., & Clay, D. 1998, J. Geophys. Res., 103, 4761
Gopalswamy, N., Yashiro, S., Kaiser, M. L., Howard, R. A., & Bougeret, J.-L. 2001, J. Geophys. Res., 106, 29219
Gosling, J. T., Hildner, E., McQueen, R. M., Munro, R. H., Poland, A. I., & Ross, C. L. 1976, Sol. Phys., 48, 389
Guhathakurta, M., & Fisher, R. 1995, Geophys. Res. Lett., 22, 1841
Harrison, R. A., et al. 1995, Sol. Phys., 162, 233
Heinzel, P., & Karlický, M. 1987, Sol. Phys., 110, 343
Heyvaerts, J., & Priest, E. R. 1976, Sol. Phys., 47, 223
Howard, R. A., Sheeley, N. R., Jr., Koomen, M. J., & Michels, D. J. 1985, J. Geophys. Res., 90, 8173
Hundhausen, A. J., Burkepile, J. T., & St. Cyr, O. C. 1994, J. Geophys. Res., 99, 6543
Hyder, C. L., & Lites, B. W. 1970, Sol. Phys., 14, 147
Innes, D. E., et al. 1999, Sol. Phys., 186, 337
Isenberg, P. A., Forbes, T. G., & Démoulin, P. 1993, ApJ, 417, 368
Ko, Y.-K., Raymond, J. C., Li, J., Ciaravella, A., Michels, J., Fineschi, S., & Wu, R. 2002, ApJ, 578, 979
Kohl, J. L., et al. 1995, Sol. Phys., 162, 313
Kopp, R. A., & Pneuman, G. W. 1976, Sol. Phys., 50, 85
Lenz, D. D., Lou, Y.-Q., & Rosner, R. 1998, ApJ, 504, 1020
Li, J., Jewitt, D., & LaBonte, B. 2000, ApJ, 539, L67
Lin, J. 2002, Chinese J. Astron. Astrophys., 2, 539 (Lin02)
Lin, J., & Forbes, T. G. 2000, J. Geophys. Res., 105, 2375 (LF00)
Lin, J., Forbes, T. G., Priest, E. R., & Bungey, T. N. 1995, Sol. Phys., 159, 275
Low, B. C. 2001, J. Geophys. Res., 106, 25141

MacQueen, R. M., & Fisher, R. R. 1983, Sol. Phys., 89, 89
Manchester, W. B., IV, Gombosi, T. I., Rouseev, I., De Zeeuw, D. L., Sokolov, I. V., Powell, K. G., Toth, G., & Opher, M. 2003, J. Geophys. Res., submitted
Martin, S. F. 1973, Sol. Phys., 31, 3
Masuda, S., Kosugi, T., Hara, H., Tsuneta, S., & Ogawara, Y. 1994, Nature, 371, 495
Mazzotta, P., Mazzitelli, G., Colafrancesco, S., & Vittorio, N. 1998, A&AS, 133, 403
McCabe, M. K. 1973, Sol. Phys., 30, 439
McKenzie, D. E., & Hudson, H. S. 1999, ApJ, 519, L93
McTiernan, J. M., Kane, S. R., Loran, J. M., Lemen, J. R., Acton, L. W., Hara, H., Tsuneta, S., & Kosugi, T. 1993, ApJ, 416, L91
Mikić, Z., & Linker, J. A. 1994, ApJ, 430, 898
Noci, G., Kohl, J. L., & Withbroe, G. L. 1987, ApJ, 315, 706
Parenti, S., Bromage, B. J. I., Poletto, G., Noci, G., Raymond, J. C., & Bromage, G. E. 2000, A&A, 363, 800
Priest, E. R. 1982, Solar Magnetohydrodynamics (Dordrecht: Reidel)
Priest, E. R., & Forbes, T. G. 2000, Magnetic Reconnection: MHD Theory and Applications (Cambridge: Cambridge Univ. Press)
Raymond, J. C. 1999, Space Sci. Rev., 87, 55
Raymond, J. C., et al. 1997, Sol. Phys., 175, 645
Riley, P., Linker, J. A., Mikić, Z., Odstrcil, D., Pizzo, V. J., & Webb, D. F. 2002, ApJ, 578, 972
Rust, D. M., & Bar, V. 1973, Sol. Phys., 33, 445
Sakao, T., et al. 1992, PASJ, 44, L83
Schmieder, B., Forbes, T. G., Malherbe, J. M., & Machado, M. E. 1987, ApJ, 317, 956
Schmieder, B., Heinzel, P., Wiik, J. E., Lemen, J., & Hiei, E. 1996, Adv. Space Res., 17, 111
Sittler, E. C., & Guhathakurta, M. 1999, ApJ, 523, 812 (SG99)
Smith, S. F., & Ramsey, H. E. 1967, Sol. Phys., 2, 158
St. Cyr, O. C., Burkepile, J. T., Hundhausen, A. J., & Lecinski, A. H. 1999, J. Geophys. Res., 104, 12493
St. Cyr, O. C., et al. 2000, J. Geophys. Res., 105, 18169
Strachan, L., Panasyuk, A. V., Dobrzycka, D., Kohl, J., Noci, G., Gibson, S. E., & Biesecker, D. A. 2000, J. Geophys. Res., 105, 2345
Švestka, Z. 1976, Solar Flares (Dordrecht: Reidel)
———. 1996, Sol. Phys., 169, 403
Švestka, Z., Fontenla, J. M., Machado, M. E., Martin, S. F., Neidig, D. F., & Poletto, G. 1987, Sol. Phys., 108, 237
Sylwester, J., Lemen, J. R., Bentley, R. D., Fludra, A., & Zolcinski, M.-C. 1998, ApJ, 501, 397
Tsuneta, S. 1993, in IAU Colloq. 141, The Magnetic and Velocity Fields of Solar Active Regions, ed. H. Zirin, G. Ai, & H. Wang (ASP Conf. Ser. 46; San Francisco: ASP), 239
———. 1996, ApJ, 456, 840
Tsuneta, S., Hara, H., Shimizu, T., Acton, L. W., Strong, K. T., Hudson, H. S., & Ogawara, Y. 1992, PASJ, 44, L63
Webb, D. F., Burkepile, J., Forbes, T. G., & Riley, P. 2003, J. Geophys. Res., submitted
Withbroe, G. L. 1978, ApJ, 225, 641
Wu, S. T., Andrews, M. D., & Plunkett, S. P. 2001, Space Sci. Rev., 95, 191
Yokoyama, T., Akita, K., Morimoto, T., Inoue, K., & Newmark, J. 2001, ApJ, 546, L69
Young, P. R., Del Zanna, G., Landi, E., Dere, K. P., Mason, H. E., & Landini, M. 2003, ApJS, 144, 135
Zhang, J., Dere, K. P., Howard, R. A., Kundu, M. R., & White, S. M. 2001, ApJ, 559, 452